THE EFFECTS OF REHABILITATION INTERVENTIONS ON HIND LIMB KINEMATICS IN A RAT MODEL OF OSTEOARTHRITIS

A Thesis
Presented to
The Academic Faculty

By

Kevin Michael Hetzendorfer

In Partial Fulfillment
Of the Requirements for the Degree
Master of Science in Bioengineering

Georgia Institute of Technology

August, 2017

THE EFFECTS OF REHABILITATION INTERVENTIONS ON HIND LIMB KINEMATICS IN A RAT MODEL OF OSTEOARTHRITIS

Approved by:

Dr. Young-Hui Chang, Advisor
School of Biological Sciences
Georgia Institute of Technology

Dr. Daniel Goldman
School of Physics
Georgia Institute of Technology

Dr. Aaron Young
School of Mechanical Engineering
Georgia Institute of Technology

Date Approved: June 28, 2017

To my parents – I surely would have never made it this far without the two of you

And to me – You helped too

ACKNOWLEDGEMENTS

First and foremost, I would like to thank my family for raising and loving me to this point. Mom and Dad, you did an amazing job getting me here and I am eternally grateful. Eric, you've been the best big brother a little brother could ask for. To all my grandparents, both living and passed, I thank you all for your love and care and support. And to Pat Cruisemire, thank you for helping me grow into the man I am now.

I would like to thank my lab mates for your help and support. All those lab meetings have finally paid off! Your feedback and critiques have been important to me. To my successor, Elana Cooper, thank you for being great company and a great friend as we struggled through this incredible workflow. To Emily Simonds, thank you for being there through the long, sleepless nights of thesis writing; I wouldn't have been able to finish without you. To Lauren O'Hara, thank you for being the best undergrad a grad student could ask for! To Elise Cade, thank you for all your work at the start of this project.

To Drs. Nick Willet and Liang-Ching Tsai, thank you for your guidance on this project. To Laura Paige, thank you for helping me through the administrative struggles of grad school and for lending an ear. To all the XROMM folks at Brown, Beth Brainerd, Steve Gatesy, and more, thank you for setting up the groundwork for an amazing technology and for arranging a great training seminar. To Daniel Miranda, thank you for the feedback on Autoscoper; it helped a good amount in figuring out how to use it. To Jay Bauman, thank you for giving me shoes to fill.

To my committee, I appreciate your time and effort in critiquing, reviewing, and questioning this thesis. To Dr. Chang, thank you for taking on a lost master's student who had no idea what he was doing and for being a great support figure.

...and I thank YOU, the reader, for keeping my memory alive.

TABLE OF CONTENTS

LIST OF TABLES

LIST OF FIGURES

LIST OF SYMBOLS AND ABBREVIATIONS

OA	Osteoarthritis
MMT	Medial Meniscal Tear
MCL	Medial Collateral Ligament
II	Image Intensifier
SID	Source to Image-Receptor Distance
XROMM	X-ray Reconstruction of Moving Morphology
DRR	Digitally Reconstructed Radiograph
ICC	Intra Class Correlation
MTP	Metatarsophalangeal
JCS	Joint Coordinate System

SUMMARY

Osteoarthritis (OA) is a degenerative joint disorder with the knee being the most common large joint affected by it. Knee OA has effects on gait patterns and these effects can change depending on the severity of the disease. Testing rehabilitation interventions for knee OA can provide an understanding of possible preventative measures. Animal models, such as the rat medial meniscal tear (MMT) model, have been used in testing interventions. Two interventions, exercise and immobilization, were applied to the rat MMT injury model. A custom biplanar X-ray video system was chosen to measure the kinematics of the experimental rats and quantify the effects of the interventions. Prior to use, workflows needed to be developed for this system. Additionally, the system needed to be validated and an appropriate analysis technique for the knee OA study needed to be chosen. An XMALab workflow reliant on manual recognition of joint centers and an Autoscoper workflow using 3D models of subject-specific bones were developed. The system's accuracy and precision values were measured using phantoms of known length. Qualitative and quantitative differences between the two workflows were compared and the Autoscoper workflow was chosen for the knee OA study. Fourteen rats were organized into four experimental groups: a non-intervention, an exercise intervention, an immobilization intervention, and a sham surgery group. The kinematic and spatiotemporal parameters were measured at three gait cycle events. Hip abduction results indicated the non-intervention group developed mild OA, while hip abduction and knee varus rotation results indicated the exercise intervention group developed advanced OA. The immobilization group results were indistinguishable from atrophic changes.

CHAPTER 1

INTRODUCTION

Osteoarthritis (OA) is a degenerative joint disorder and the most common type of arthritis in the Western world [1] [2] [3]. This disorder is characterized by a degeneration of the articular cartilage in the affected joint, but is generally defined by a presentation of symptoms or pathologies [2] [3]. The knee is the most prevalent large joint affected by OA, causing many clinical symptoms in elderly populations [1] [4]. The Framingham osteoarthritis study showed that knee OA increased from an average of 27% in subjects between the ages of 60 and 70 to an average of 44% in subjects between the ages of 80 and 92, showing a clear increase in occurrence with age [4]. As the human population grows, more people will experience the effects of knee OA prompting more research to focus on it. The main causes for knee OA development are not entirely understood, but dynamic joint loading and excessive forceful impact have been identified as mechanical contributors [5] [6]. The chronic musculoskeletal pain and functional disability resulting from knee OA causes reduced quality of life and increased risk of death, which has made it a major disease in the elderly around the world [1] [7].

Biomechanically, the presentation of gait patterns induced by knee OA vary based on the severity of the disease [5]. Knee flexion angles during stance phase can decrease with increasing knee OA severity and a varus rotation at the knee can increase over time due to its self-perpetuating nature (varus rotation is a lateral tilt of the tibia; tilt causes more wear on the medial condyle of the tibia leading to more tilt) [5] [6]. Treatments can be categorized as either non-pharmacological (information, quality of life changes,

physical therapy, or aerobic exercise), pharmacological (non-steroidal anti-inflammatory drugs or topical treatments), or invasive (intra-articular injections or joint-replacement surgery) [1] [7]. These treatments aim to reduce joint pain, to improve function and mobility, to educate the affected person about knee OA management, and to prevent or slow the progression of the disease [1] [7]. By testing different rehabilitation strategies for knee OA, an understanding of possible preventative measures can be gained. Animal models of OA have historically been used in testing interventions [8] [9]. The surgically-induced rat medial meniscal tear (MMT) knee OA model results in predictable morphological changes similar to those in human OA, while having significantly faster cartilage degeneration which allows for OA to develop quicker for expedited testing [8].

The rat MMT model, as described by Bendele, consists of two surgical events: a transection of the medial collateral ligament (MCL) near its connection to the meniscus, and a cut of the meniscus at its narrowest point [8]. Inducing these injuries causes a rapid progression of cartilage degeneration leading to knee OA [8] [10]. Rats with OA in one limb develop unilateral gait compensations, spending more time on their contralateral limb [10] [11]. The controlled nature of this model allows for experimentation on potential causes of OA and for testing possible interventions. Focusing on gait changes, the question of how to test the efficacy of these interventions and how to quantify their results arises.

Regarding interventions to test, repetitive loading and reduced loading are of interest. Repetitive loading can be induced by elevated levels of exercise in rats. In human OA studies, repetitive loading, such as regular aerobic, joint specific, and range of motion exercises, has been shown to help reduce pain [1] [7]. Non-physiological loading,

such as high-impact forces, can lead to preexisting OA becoming more severe [12]. Repetitive joint loading has also been shown to be a cause of knee OA [6] [12]. This intervention can be tested by having MMT rats perform specific levels of exercise to see if the regimen alleviates or aggravates the OA. How to quantify these results will be discussed in the next paragraphs. Reduced loading can be induced by immobilization of the rat hind limb. Joint immobilization is typically used as a treatment for joint injuries [13]. However, studies in humans and in dogs have shown that joint immobilization can cause articular cartilage degeneration and decreased cartilage thickness [13] [14]. Another study described immobilization as a way that "induces atrophic changes within articular cartilage that superficially mimic OA pathology" [15]. None of these studies have looked at the effects of immobilization on the MMT model. The goal of this intervention is to measure if the lack of loading on and movement of the hind limb exacerbates or stalls the knee OA.

A detailed review of gait analysis methods used in rat OA models was compiled by Allen et al. [16]. Paw print analysis through toe spacing and paw print lengths can be used in nerve functionality indices (sciatic, tibial, and peroneal) [16]. Differences in paw print areas or intensities can lead to weight-bearing analyses [16]. Spatial characteristics, such as step length and width or stride length, provide geometric data about a rat's gait, while temporal characteristics, like stance time and stride time, can describe the sequence and timing of limb movements [16]. Grouping the two together, these spatiotemporal characteristics can describe asymmetries in a rat's gait and thoroughly list the end-point (toes) locations at any time [16]. Spatiotemporal analysis is frequently used with systems capable of tracking paw print location [10] [11] [17] [18]. Measuring ground reaction

forces utilizing force plate-integrated walkways is one method for dynamic gait analysis [10] [17]. Readouts of peak vertical ground reaction forces would be able to distinguish limbs that are not experiencing full body weight. This would help with rat OA analyses as a limb with OA would be expected to have a smaller vertical ground reaction force [10].

3D kinematics can quantify the fine translations and rotations involved in locomotion [16]. In rats, however, skin movement errors make accurate hind limb kinematics difficult to measure using standard optics [19]. High-speed X-ray video avoids this issue by directly measuring limb skeletal movements [19]. A review of the literature yielded few results on the use of X-ray video to measure rat OA joint kinematics. Boettger et al. used a single-plane (2D) X-ray system from a sagittal view to measure rat OA knee flexion and extension [20]. However, accurate 3D kinematics from X-ray video requires a high-speed biplanar videoradiography system, a technology that has not yet been adopted by many research laboratories [21] [22].

Utilizing a custom-built high-speed biplanar videoradiography system, this thesis proposes to measure the kinematic changes in gait resulting from interventions in an MMT model of rat OA. This will be accomplished in three main steps.

1. *Implement and characterize a high-speed biplanar videoradiography system*

Before this customized and innovative system can be used extensively in rats, X-ray motion analysis workflows describing its use must be developed and its capabilities must be determined. Developing workflows for this system will allow users to record high-speed biplanar X-ray videos and digitize the information in them. Kinematic data will then be derived from these digitized files. Characterizing the capabilities of the system will determine the accuracy and precision it can achieve, quantifying the

performance. Additionally, user precision from digitizing the X-ray video information will need to be quantified in order to record any potential sources of error.

2. *Compare 3D X-ray motion analysis techniques*

With the system's workflows implemented, an appropriate kinematic analysis for the OA study will need to be identified. The capabilities of two potential software methods (XMALab and Autoscoper) need to be determined and understood. Comparing their qualitative aspects and quantifying any kinematic differences between them will provide the insight needed to choose the appropriate methodology for the next aim in this thesis.

3. *Analyze the effects of two different rehabilitation interventions for knee osteoarthritis on rat hind limb joint kinematics*

After the system has been implemented, characterized, and an appropriate X-ray motion analysis workflow has been chosen, joint kinematics can be measured. A set of rats will be randomly grouped as either intervention subjects or control subjects. Once OA has been induced in all groups, interventions will be applied to select groups and given time to take effect. The rats' gaits will then be analyzed using a high-speed biplanar videoradiography system and the kinematic differences between the groups will be statistically compared. Marker implantation will not be utilized in order to avoid any possible interaction effects resulting from marker implantation procedures.

Measuring the joint kinematics of the experimental groups should provide insight into the effectiveness of the interventions. My general hypothesis is that kinematic differences will be found between testing groups as a result of the different interventions.

Additionally, I hypothesize that these kinematic differences will generally strengthen the applicability of the rat MMT model to human knee osteoarthritis.

CHAPTER 2

IMPLEMENTATION AND CHARACTERIZATION OF A BIPLANAR HIGH-SPEED VIDEORADIOGRAPHY SYSTEM FOR RAT KINEMATICS

2.1 Introduction

For the purposes of the studies in this thesis, a custom biplanar high-speed videoradiography system designed and built by Imaging Systems and Service, Inc. (Painesville, Ohio) was utilized and, from this point forward, will be referred to as "the system". The system consists of two X-ray tubes and emitters, two collimators, two high-speed digital video cameras (Xcitex XC-2M), two image intensifiers (IIs, 12" diameter), several control units, a synchronized timing unit, two X-ray control panels, a collimator control panel, a dedicated user computer, and other assorted components. The X-ray tubes, emitters, and collimators are mounted on two columns, each supported by wide wheeled platforms. The IIs and high-speed cameras are mounted on two similar columns, each in line with an X-ray emitter. The four columns are connected by adjustable overhead struts that keep the X-ray emitters/collimators in line with the IIs/cameras and allow for a modifiable source to image-receptor distance (SID). The wheeled platforms the columns are mounted on allow movement of each set of columns, which in turn lets the user adjust the angle between the two X-ray beams. On each column, the emitter/collimator or II/camera unit can be moved vertically and locked into place. Existing safety protocols do not permit system operation if an emitter is not in line with its II. The system's layout is displayed in Figure 2.1.

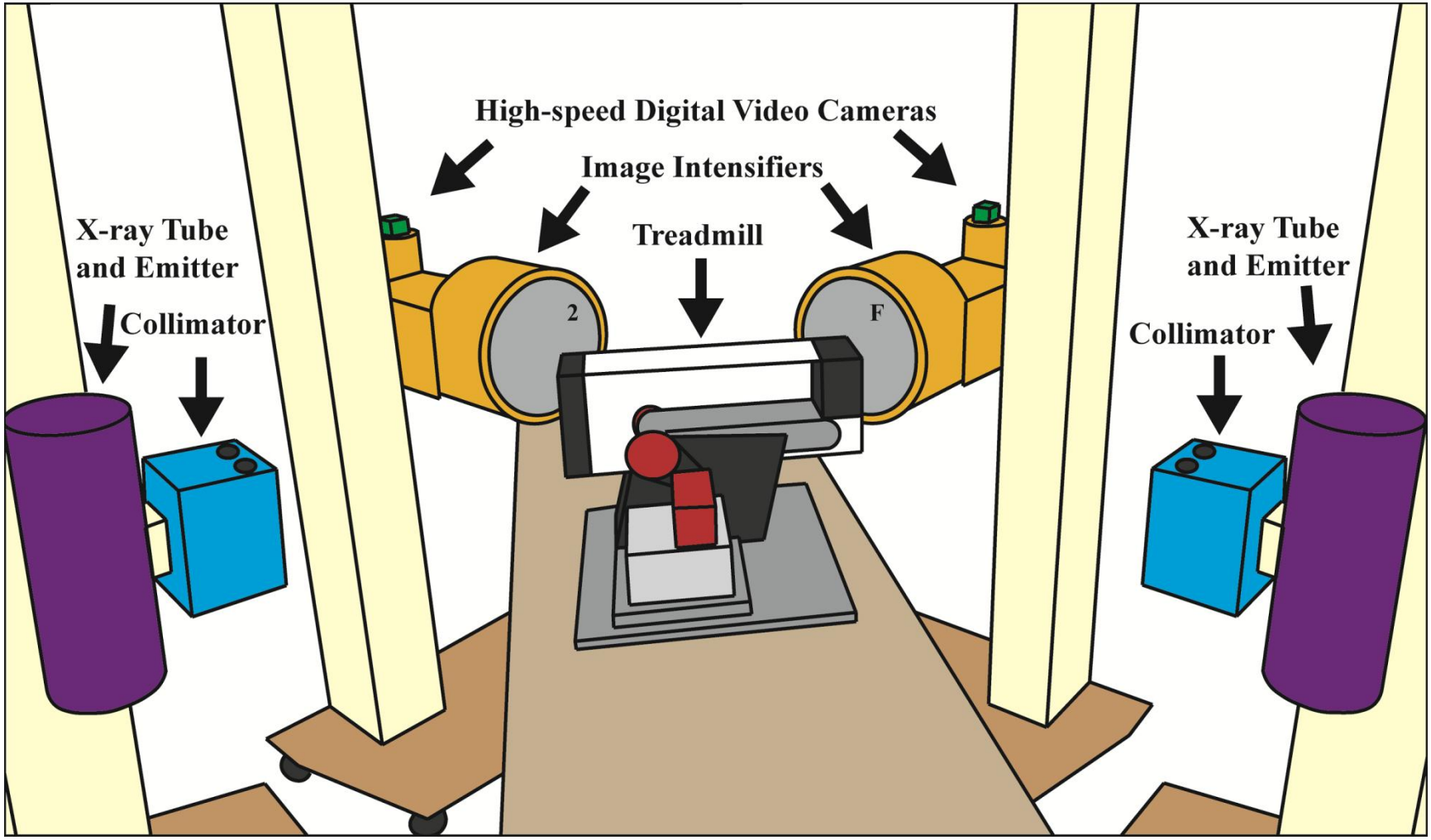

Figure 2.1: Diagram of the custom biplanar high-speed videoradiography system, with a treadmill in the imaging volume

The settings of the X-ray generators were determined after several test trials, optimizing them for the desired visibility of a rat hind limb – 42 kV (controls image contrast), 80 mA (controls image brightness/intensity), 5 ms exposure time, a pulsed (strobe) X-ray mode, 5 ms camera shutter speed, 1920 x 900 image resolution, and a 100 Hz frame rate with a 6 second video duration. The resulting X-ray videos show a capture volume approximately the size of a soccer ball when at standard magnification. Each II also has a lead shape taped onto its surface, hard-coding an identifiable mark (the letter F or the number 2) onto the side of each X-ray video.

In order to use the system for rat kinematics, a workflow needed to be implemented. This workflow would lead the user through the process of calibrating the capture volume, taking X-ray videos, manually tracking hind limb motion, calculating joint kinematics from the motion, and exporting these data. After determining an appropriate system workflow, the system's accuracy and precision needed to be quantified. These values would provide baseline accuracy and precision for all future studies utilizing this system. Additionally, because the workflow relies on manual tracking of hind limb motion, user precision needed to be evaluated to determine how this can affect kinematic data.

2.2 Methodology

2.2.1 Workflow Implementation

The X-ray Reconstruction of Moving Morphology (XROMM) development project at Brown University has previously described a workflow for marker-based X-ray kinematics [23]. This process requires three radio-opaque beads to be affixed onto all bones of interest. X-ray images of a known volume are then taken to calibrate the

imaging space. After recording the X-ray videos, the bones are scanned in a CT scanner with the beads still implanted. The beads are automatically identified and tracked throughout the videos using a marker tracking software, XMALab (Brown University, Providence, Rhode Island). The tracking data, consisting of xyz coordinates of the markers, are imported into an animation software, Maya (Autodesk, San Rafael, California), where 3D models of the beads are animated by the data. Since the positions of the beads relative to the bones are known from the CT scans, 3D models of the bones are able to be overlaid onto the beads, applying the animation to the bone models. Using the 3D models of the bones, anatomical joint coordinate systems (JCSs) can be defined for each bone, translating the animation data into joint position and rotation data.

In order to adhere to a markerless tracking method, the XROMM marker-based XMALab workflow needed to be modified before it could be adopted. Since no markers are used, there are no beads to be automatically identified and tracked, which means the 3D bone models are not able to be animated. Manually identifying three anatomical landmarks accurately and precisely for each bone of interest in a rat hind limb from X-ray videos would be out of the range of this system's technical capabilities, as well as the user's capabilities. Manually identifying the center of a joint is more feasible. By manually tracking the locations of the joints in a rat hind limb, the xyz coordinates of the joint centers were exported. Using trigonometry and geometry, the xyz coordinates were then transformed into joint angles.

Markerless XROMM techniques also exist in the forms of scientific rotoscoping and the use of the Autoscoper software (Brown University, Providence, Rhode Island) [21] [24]. Gatesy et al. describe scientific rotoscoping as a method of motion analysis that

uses skeletal models to extract 3D kinematics from a combination of X-ray and standard optics and renders animations with high accuracy [21]. This method does not require implanted radio-opaque markers to track motion, but rather uses the skeletal models themselves to track the motion. A 3D environment of the X-ray and standard cameras is created using a known calibration volume. The skeletal models are generated from CT scans and are manually oriented and positioned in the environment such that they align with both the X-ray and standard cameras accurately. JCSs are then attached to the skeletal models, transforming the model movement into joint position and rotation data. In a different manner from scientific rotoscoping, the Autoscoper software utilizes digitally reconstructed radiographs (DRRs) from CT scans of bones to determine 3D kinematics from biplanar X-ray videos. Miranda et al. describe Autoscoper as having an auto-registration algorithm that uses contrast enhancement and Sobel edge detection to align bone DRRs with the X-ray videos [24]. Over the course of this thesis work, the auto-registration function of Autoscoper has been found to not be an efficient way to find bone movements and rotations. Manual registration with Autoscoper was found to work well, especially in tandem with the software's built-in filter capabilities that help with visually identifying bone shapes and markings. Autoscoper does not have an innate way to define an anatomical JCS, meaning its rigid body motion data would need to be transformed into joint kinematics outside of the software.

To utilize Autoscoper's biplanar X-ray video registration capabilities, aspects of the scientific rotoscoping technique were integrated into the procedure, namely the use of a 3D environment. With this, the rigid body motion data exported from Autoscoper was imported into the 3D environment, generated by Maya, and applied to the corresponding

bone model. Anatomical JCSs were applied to the bone models, transforming the motion data into joint data.

Two markerless tracking techniques were incorporated into the system's workflow: a markerless application of XMALab using manual tracking of joint centers, and an application of scientific rotoscoping with Autoscoper, using manual tracking of bone models. The system's workflow was finalized with the inclusion of these two techniques.

Before data collections, the X-ray volume calibration object is built. A custom-build acrylic calibration cube with 64 steel spheres (3 mm diameter), evenly distributed 5 cm apart in perpendicular directions, was designed and built [23]. Lead shapes are overlaid onto four different spheres to act as identifiable points during volume calibration. Images of this cube are taken during collections. Additionally, image distortion needs to be accounted for. X-ray image intensifiers can come with image artifacts, like pincushion distortion (a geometric, nonlinear magnification across the image) or S distortion (an S-shaped distortion across the image) [23] [25]. Distortion correction is completed by taking X-ray images of an equally distributed pattern. In this case, perforated metal sheets were affixed to the IIs (part number 9255T641, McMaster-Carr, Robinson, New Jersey) [23]. After data collections, the images of the metal sheets (undistortion images), the images of the calibration cube (calibration images), and the X-ray videos are imported into XMALab. Once in the software, XMALab uses a distortion correction algorithm with the undistortion images to remove the distortion from the images and videos [23]. Next, the identifiable markers on the calibration images are selected in XMALab and calibration matrices are generated for the system's

configuration. At this point, the workflow splits between the two techniques described earlier.

Continuing with the markerless XMALab technique, the software allows the user to manually identify points in both X-ray videos simultaneously. This is completed for all joint centers of interest at the appropriate gait cycle events. Global coordinates are taken into account in the software. The global "vertical" is derived from the z-direction on the calibration cube. The global "forward" is derived from a consistent motion during the X-ray videos, such as a foot planted on a treadmill moving through time. With "vertical" and "forward" defined, as well as the xyz coordinates of joint centers, the data are exported from XMALab and imported into any spreadsheet software (Microsoft Excel). In Excel, the data are transformed using applications of trigonometry and geometry into joint rotations.

Continuing with the Autoscoper technique, the undistorted X-ray videos are exported out of XMALab with the calibration matrices as TIFF-format stacks. CT scans of the bodies of interest are performed, generating DICOM-format files for each scan. These DICOM files are imported into 3D Slicer (Fedorov A., et al.), an open source medical image processing software. In 3D Slicer, the DICOM files are carefully converted to the correct coordinate system and the bone images are manually segmented from each other. Once segmented, the bone images are also converted into a 3D surface model. The image stacks and 3D surface models are exported for each bone. The image stacks then need to be converted to work with Autoscoper. This is done using ImageJ (NIH Image), an open source image processing software. The 3D surface models also need to be converted, in this case using MeshLab (Cignoni P., et al.). The converted

image stacks are then imported into Autoscoper, along with the undistorted X-ray videos, calibration matrices, and voxel size information from 3D Slicer. The software allows the user to apply filters to the bone DRR (generated from the image stack) and to the X-ray videos to allow for more accurate registration. The user then rotates and positions the bone DRR manually in both X-ray videos and saves the key frame. This is completed for all bones of interest at the appropriate gait cycle events. Once complete, the rigid body motion data is exported from Autoscoper. In Maya, the 3D bone surface models are imported and, using anatomical landmarks, a JCS is carefully applied to each bone. Using a Maya XROMM toolbar (Brown University, Providence, Rhode Island), the 3D environment is set up with virtual cameras and real-time playbacks of the X-ray videos. The motion data are then applied to each 3D bone model. After updating the JCSs with motion data, joint data are exported. Figure 2.2 shows a diagram of the finalized workflow, including both markerless tracking techniques.

2.2.2 System Accuracy and Precision

The accuracy and precision of the system were measured based on a method previously described by Knorlein et al. [26]. Four phantoms were built, each with two steel spheres (5 mm diameter) implanted in them at set distances from each other. Each phantom was placed on a treadmill in the imaging volume, set at three different speeds (38.333 mm/s, 43.333 mm/s, and 50.000 mm/s). For each speed, the positions of the spheres on the phantom were tracked for approximately 600 frames of motion. In total, 7200 frames of tracking were used for system validation.

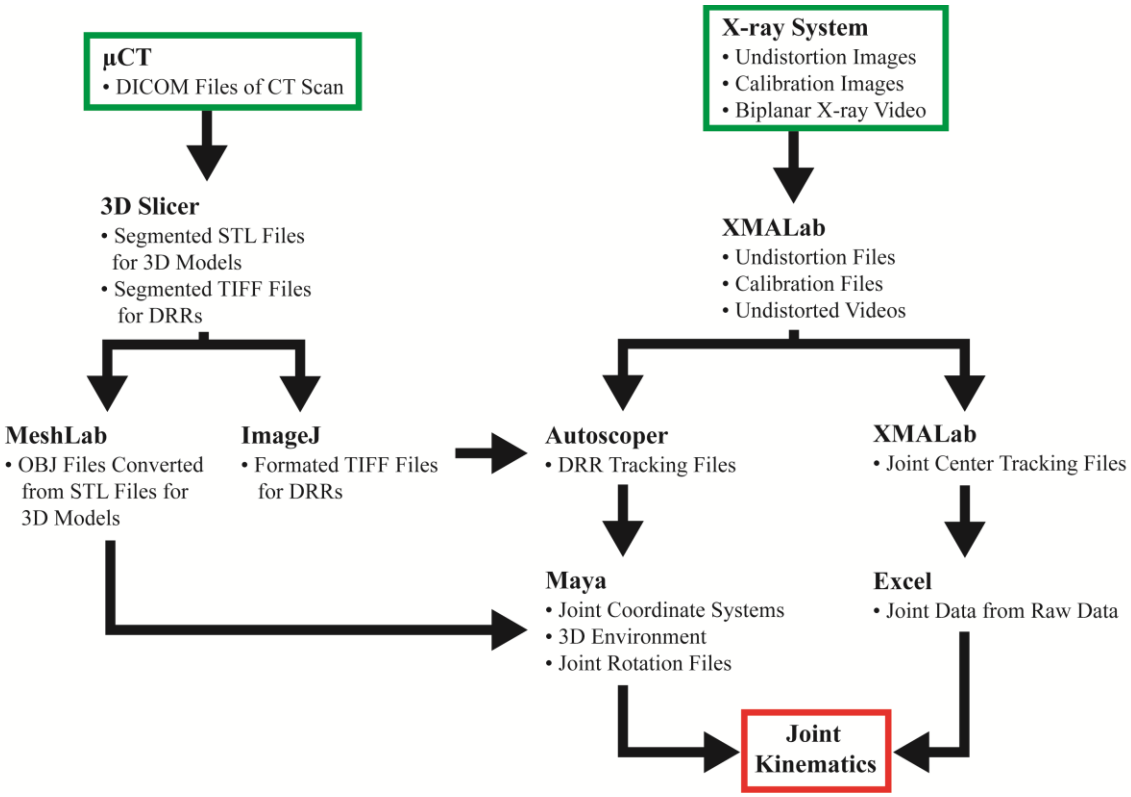

Figure 2.2: Workflow showing the process from data collection (green boxes) to exported data (red box). Both the Autoscoper workflow and the XMALab workflow are included

Three phantoms were built out of LEGO bricks. These were used due to their high manufacturing tolerance (0.002 mm) [27]. The steel spheres were pushed into the bottom center hole on two LEGO bricks and the phantoms were constructed such that the spheres were approximately a given distance apart (16 mm, 32 mm, and 64 mm). The fourth phantom was created from a 2.9 cm x 4.7 cm block of polypropylene. A CNC (0.005 mm precision) was used to make two 5 mm diameter holes 2.5 mm deep in the block, approximately 38.1 mm apart. The spheres were then placed in the holes and sealed with a Loctite adhesive. The phantoms can be seen in Figure 2.3.

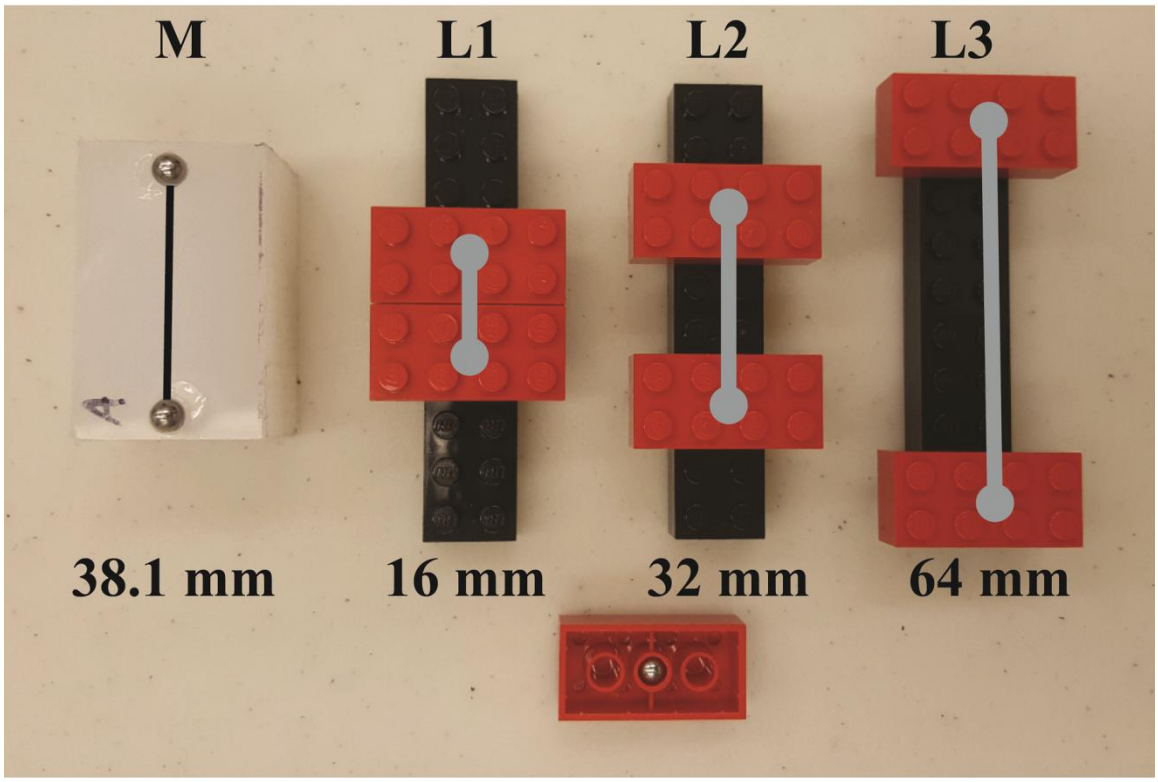

Figure 2.3: Manufactured phantom and LEGO brick phantoms used for system validation, with an additional LEGO brick detailing marker location

For this system validation, the X-ray beams were oriented approximately 90° from each other. After collecting X-ray videos of the four phantoms, the videos were analyzed in XMALab. The software's automatic marker recognition algorithm was used to track the steel spheres. The xyz coordinates of the spheres were then exported and the distances between them were analyzed.

2.2.3 User Precision

Due to the manual tracking nature of XMALab and Autoscoper, as described in the workflow, the user's precision needs to be accounted for. X-ray video frames from Chapter 4 were used in this user precision study. A frame of gait during rat locomotion on a treadmill (toe off) was selected from 14 rats. As described by Bonnan and Gatesy,

these frames were then manually tracked ten times [21] [28]. Because the system's workflow accounts for two different markerless tracking techniques, this manual tracking was performed for both XMALab and Autoscoper. As further described in Chapter 3, in the context of rat hind limb kinematics, XMALab requires the tracking of four joint centers and Autoscoper requires the tracking of three bone DRRs. XMALab produces four joint angles and Autoscoper produces nine joint angles. In terms of tracking for user precision, a total of 560 XMALab joint centers and 420 Autoscoper key frames were tracked.

The resulting angular data from the ten trials for the 14 rats were compared. An intra class correlation (ICC) statistical analysis for absolute agreement (ICC(3,1)) was performed on the data for each technique and angle. ICC values greater than 0.90 show a consistent agreement, at clinical levels, across the measurements [29]. Additionally, the standard deviations of each angle for each rat were averaged into a table of grand means of standard deviations.

2.3 Results

The system accuracy and precision values are compiled in Table 2.1 with the detailed results in Table A.1. Accuracy error refers to the absolute value of the difference between the known value (16, 32, and 64 mm) and the measured value. Precision refers to the standard deviation of the values at a given treadmill speed (600 values). The average accuracy error and average precision are the averages of those respective numbers across the three treadmill speeds (1800 values). L1, L2, and L3 refer to the different LEGO brick phantoms and M refers to the manufactured phantom.

Table 2.1: System accuracy and precision measured using 1800 frames of marker tracking each from four phantoms

Phantom	Average Accuracy Error (mm)	Average Precision (mm)
L1 (16.000±0.002 mm)	0.105	0.058
L2 (32.000±0.002 mm)	0.042	0.071
L3 (64.000±0.002 mm)	0.113	0.099
M (38.100±0.005 mm)	0.226	0.066

The average accuracy error values for the LEGO brick phantoms are around 0.1 mm, with the second LEGO phantom having an average error near 0.04 mm. The LEGO phantoms follow a linear relationship with their average precision values, starting at 0.058 mm for the 16 mm phantom and increasing to 0.099 mm for the 64 mm phantom. The manufactured phantom has an average accuracy error roughly twice that of the LEGO phantoms, near 0.2 mm, with a comparable average precision of 0.066 mm. The average accuracy error of the three LEGO phantoms is approximately 0.087 mm with an average precision of 0.076 mm. Accounting for all four phantoms, the average accuracy error is approximately 0.122 mm with an average precision of 0.073 mm. The minimum accuracy error encountered during this validation study was from the L2 phantom at 38.333 mm/s and was approximately 0.018 mm. The minimum precision encountered was from the L1 phantom at 43.333 mm/s and was 0.047 mm. Conversely, the maximum accuracy error was from the M phantom at 43.333 mm/s and was approximately 0.236 mm, while the maximum precision was from the L3 phantom at 50.000 mm/s and was 0.135 mm.

The resulting user precision ICC(3,1) values for absolute agreement were greater than 0.993 for all 14 rats, indicating clinical levels of agreement. The grand means of standard deviations for each angle using the two manual tracking methods are compiled in Table 2.2. As described in Chapter 3, the anatomical angles refer to: hip abduction and adduction, internal and external hip rotations, hip flexion and extension, knee varus and valgus rotations, internal and external knee rotations, knee flexion and extension, ankle inversion and eversion, internal and external ankle rotations, and ankle plantar flexion and dorsiflexion. The two methods, Autoscoper and XMALab, refer to which markerless tracking technique was used to quantify the angles.

Table 2.2: Average single user precision for the listed hind limb angles using 560 identified joint centers in XMALab and 420 registered key frames in Autoscoper

	Methods	
Angles	Autoscoper	XMALab
Hip Ab/Ad	0.77°	0.80°
Hip Int/Ext	3.71°	-
Hip Flex/Ex	1.33°	0.47°
Knee Var/Val	4.58°	-
Knee Int/Ext	6.52°	-
Knee Flex/Ex	1.77°	0.71°
Ankle Inv/Ev	7.63°	-
Ankle Int/Ext	4.33°	-
Ankle Flex/Ex	1.50°	0.94°

The average user precision varies for the different angles. The values quantified using XMALab are generally lower than the same values quantified using Autoscoper, indicating greater precision. In XMALab, the values are all less than one degree. In Autoscoper, the values range from 0.77° to 7.63°. Generally, in each set of angles, the flexion/extension angle has the greatest precision (1.33° Hip Flex/Ex, 1.77° Knee

Flex/Ex, 1.50° Ankle Flex/Ex). Conversely, the long-axis rotation angles in each set have the lowest precision (3.71° Hip Int/Ext, 6.52° Knee Int/Ext, 7.63° Ankle Inv/Ev).

2.4 Discussion

The system's accuracy and precision values were measured using a predefined method described by Knorlein [26]. The average results for the three LEGO brick phantoms were an accuracy of 0.087 mm and a precision of 0.076 mm, while the average results of all four phantoms were an accuracy of 0.122 mm and a precision of 0.073 mm. The machined phantom (M) had an accuracy of 0.226 mm, which is almost three times the average accuracy of the three LEGO brick phantoms. All four phantoms had similar construction precision values (L1, L2, and L3 - 0.002 mm; M - 0.005 mm), but the machined phantom's accuracy ended up being higher. This suggests an error in construction of the machined phantom, as the accuracy values should be closer. Possible errors could include: residual material in the holes the spheres were placed into, the adhesive shifting the position of the spheres slightly, or a defect in the sphere sizes leading to unequal positions. Because of this possible error, the machined phantom's accuracy value should not be taken into account for the system's overall accuracy. The consistency with which the machined phantom was measured can still be taken into account though, because a value can be precise without being accurate. Using this exclusion, the system's overall accuracy is 0.087 mm with an overall precision of 0.073 mm.

The average user precision values were measured using a method discussed by Bonnan and Gatesy [21] [28]. The calculated ICC values show an excellent level of agreement. Based on these values, it can be concluded that user precision would not

significantly affect the measured kinematic results from XMALab or Autoscoper. The grand means of standard deviations in Table 2.2 show the precision values. Generally, the standard deviations from XMALab measurements were lower than their Autoscoper counterparts. This could be due to the difficulty of precisely manipulating a complex 3D object for manual tracking in Autoscoper compared to locating the approximate center of a joint in XMALab. Looking at the values in each set of angles, the flexion and extension angles have the best precision. These angles are best viewed from a sagittal view, and the X-ray emitters and cameras were skew sagittal to the treadmill, meaning the range of motion of these angles was fully in view. Conversely, angles centered in the frontal plane were not as precisely measured as the flexion and extension angles. This includes the knee varus and valgus rotations and the ankle internal and external rotations. The hip abduction and adduction angles did not experience the same effect due to being connected to the global reference frame (as described in Chapter 3). The long-axis rotation angles were measured with the lowest precision and proved more difficult to track (hip and knee internal and external rotations, ankle inversion and eversion). Even with markers, long-axis rotation can be difficult to measure [30].

In this chapter, the high-speed biplanar videoradiography system has been described and two workflows for analyzing data from it, the XMALab method and the Autoscoper method, have been identified. The system was then validated with an accuracy and precision study using four phantoms, three made of LEGO bricks and one custom machined. User precision was measured and quantified for all angles measureable by both workflows. The resulting ICC values showed an excellent agreement between all values. Knowing this, the appropriate workflow for the knee OA study can be chosen.

The XMALab and Autoscoper methods can be compared and differences between the two methods can be quantified.

CHAPTER 3

COMPARISON OF TWO DIFFERENT 3D X-RAY MOTION ANALYSIS TECHNIQUES

3.1 Introduction

As described in Chapter 2, the system's workflow incorporates two markerless tracking techniques – XMALab and Autoscoper. The XMALab technique relies on the user manually identifying joint centers and it then uses vector geometry to calculate joint angles. The Autoscoper technique uses CT scans of a bone as a tracking tool with the user identifying anatomical landmarks. Hind limb models are then used to calculate joint angles [31] [32]. Before addressing the knee OA study in Chapter 4, the appropriate and most effective markerless tracking technique to use needed to be identified.

In the context of rat hind limb kinematics, each technique has advantages and disadvantages. Using the JCSs defined later in this chapter, the Autoscoper technique is found to produce nine joint angles, while the XMALab technique can produce four joint angles. As described earlier, Autoscoper uses anatomical landmarks from a subject-specific CT scan in its technique. XMALab does not use anatomical features directly and instead requires the user to identify joint centers. Anecdotally, the Autoscoper technique is significantly more time consuming than the XMALab technique due to the difficulty of the DRR tracking and the amount of steps and software that the user works through. As shown in Table 2.2, the user precision values quantified using XMALab are generally lower (more precise) than the values quantified using Autoscoper. This indicates that XMALab (for those four angles) can allow the user to obtain better precision than

Autoscoper.

A qualitative list of differences between the two techniques helps in the choice of methodology for application in a study. Quantifying the differences between the two, however, would provide a concrete metric with which to compare them. Using rat hind limb angles as a comparison point, the angles generated using XMALab and Autoscoper can be analyzed and significant differences in the techniques can be identified.

3.2 Methodology

The experiment design for Chapter 3 is based on the experiment design featured in Chapter 4 and an abridged description will be presented here with information relevant to this aim; the full detailed description can be found in Chapter 4.

Fourteen male Lewis rats were selected for MMT surgery to induce knee OA and to test two different intervention techniques. The rats were randomly placed into four groups: a sham surgery group (four rats, SHAM), a non-intervention group (three rats, NON), a running intervention group (three rats, RUN), and an immobilization intervention group (four rats, IMB). The left hind limb kinematics at three distinct gait cycle events were of interest: initial contact, midstance, and toe off. Rats were tested at 8 weeks post-surgery. For testing, rats were enclosed in a 21.5 x 15.0 x 56.0 cm Plexiglas treadmill (Rat Modular Treadmill, Columbia Instruments) oriented skew sagittal to both X-ray beams of the custom biplanar high-speed videoradiography system (Imaging Systems & Service, Inc., Painesville, Ohio). Rats walked on the treadmill (0.5 m/s) while X-ray videos were taken of the locomotion (100 Hz). Five gait cycles of steady locomotion were identified for each rat. After collection, rats were euthanized and CT scans were taken of the left hind limb using EPIC-μCT (100 μm resolution) to create 3D

bone surface models and bone DRRs, as described in Chapter 2. An example of a resultant 3D bone surface model of a rat hind limb can be seen in Figure 3.1. All data was collected according to a protocol approved by the Georgia Institute of Technology IACUC.

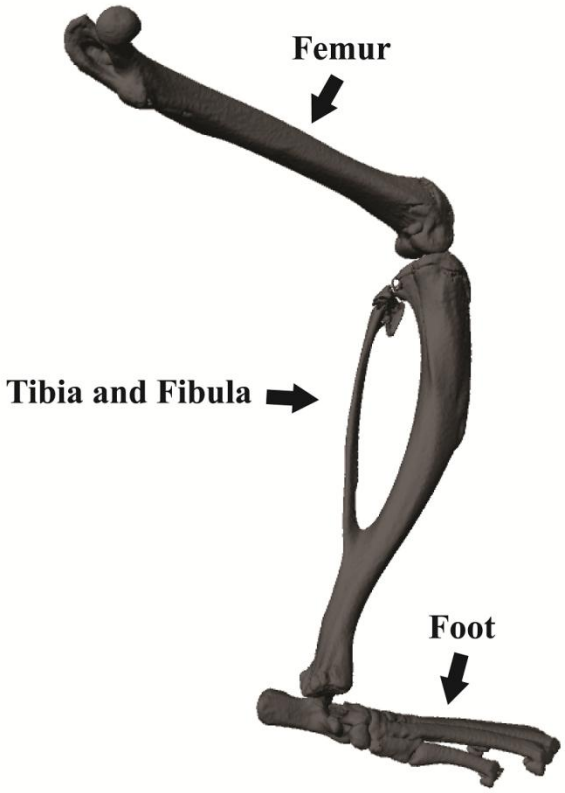

Figure 3.1: The 3D bone surface model of a rat hind limb generated from a CT scan

The X-ray videos were analyzed using the two markerless tracking techniques, as described in Chapter 2. Figure 3.2 shows the interfaces for them, with XMALab at the top and Autoscoper at the bottom. In XMALab, joint centers for the hip, knee, and ankle were tracked, as well as the toes' position. In Autoscoper, DRRs for the femur, tibia and fibula, and the foot were tracked.

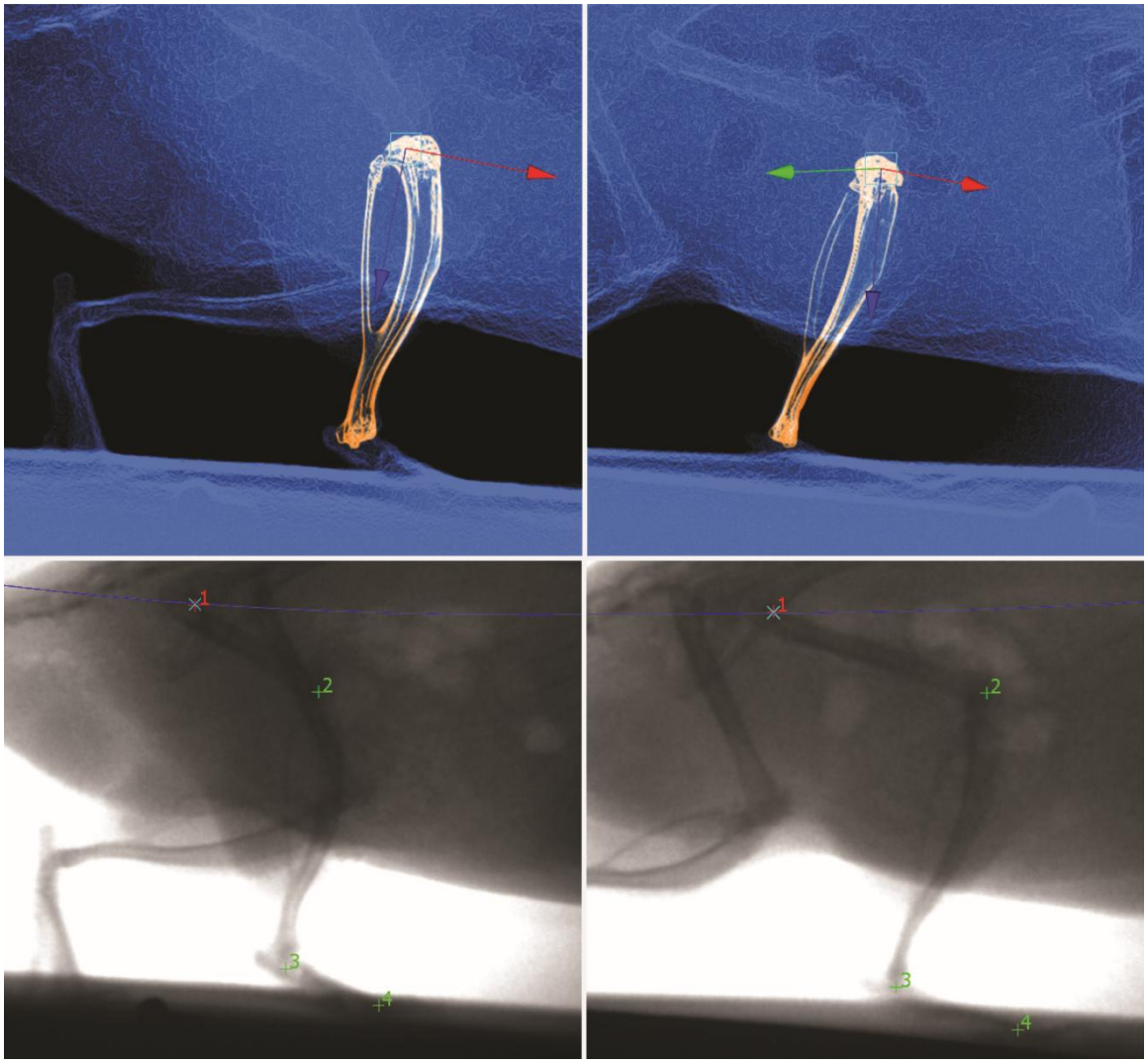

Figure 3.2: Interfaces for Autoscoper (top) and XMALab (bottom)

In XMALab, four anatomical angles were able to be quantified: hip abduction and adduction, hip flexion and extension, knee flexion and extension, and ankle plantar flexion and dorsiflexion. The hip angles are derived from the "vertical" and "forward" vectors (discussed in Chapter 2) which have a base in the hip joint center and point "vertical" (in the calibrated "vertical" direction) and point "forward" (based on a vector defined by the movement of the metatarsophalangeal or MTP joint in contact with the

treadmill over time). Hip flexion and extension is defined as the angle between the "vertical" vector and the femur vector defined by the hip joint center and the knee joint center (0° points the femur straight up, 90° lays the femur horizontal). Hip abduction and adduction is defined as the angle of projection of the femur vector onto the vertical plane containing the "forward" vector (0° points the femur directly forward, abduction is positive). Knee flexion and extension is defined as the angle between the femur vector and the tibia vector composed of the knee joint center and the ankle joint center (0° fully extends the knee, flexion is positive). Ankle plantar flexion and dorsiflexion is similarly defined as the angle between the tibia vector and the foot vector composed of the ankle joint center and the toe marker (0° has the foot perpendicular to the tibia, plantar flexion is positive).

In Autoscoper, nine anatomical angles were able to be defined: hip abduction and adduction, internal and external hip rotations, hip flexion and extension, knee varus and valgus rotations, internal and external knee rotations, knee flexion and extension, ankle inversion and eversion, internal and external ankle rotations, and ankle plantar flexion and dorsiflexion. The JCSs used to find the angles were defined based on anatomical landmarks previously described by Edgerton et al., with an adaption by Burkholder et al. at the ankle due to the talus not being present in all foot bone surface models. The femur JCS was defined by the femoral head and the medial and lateral epicondyles [31]. The tibia JCS was defined by the medial and lateral maleoli and the medial and lateral condyles [31]. The foot JCS was defined by the superior end of the calcaneus and the 2nd and 5th MTP joints [32]. The "zero pose" of all nine angles is when the three JCSs are aligned. The joint angles are then defined as the rotations of the distal body relative to the

proximal body, in a ZYX rotation sequence, with reference to the "zero poses" [23]. The hip angles are the femur JCS rotated relative to the "vertical" and "forward" vectors defined earlier. The knee angles are the tibia JCS rotated relative to the femur JCS. Finally, the ankle angles are the foot JCS rotated relative to the tibia JCS. Figure 3.3 depicts both the angles defined using XMALab and the angles defined using Autoscoper.

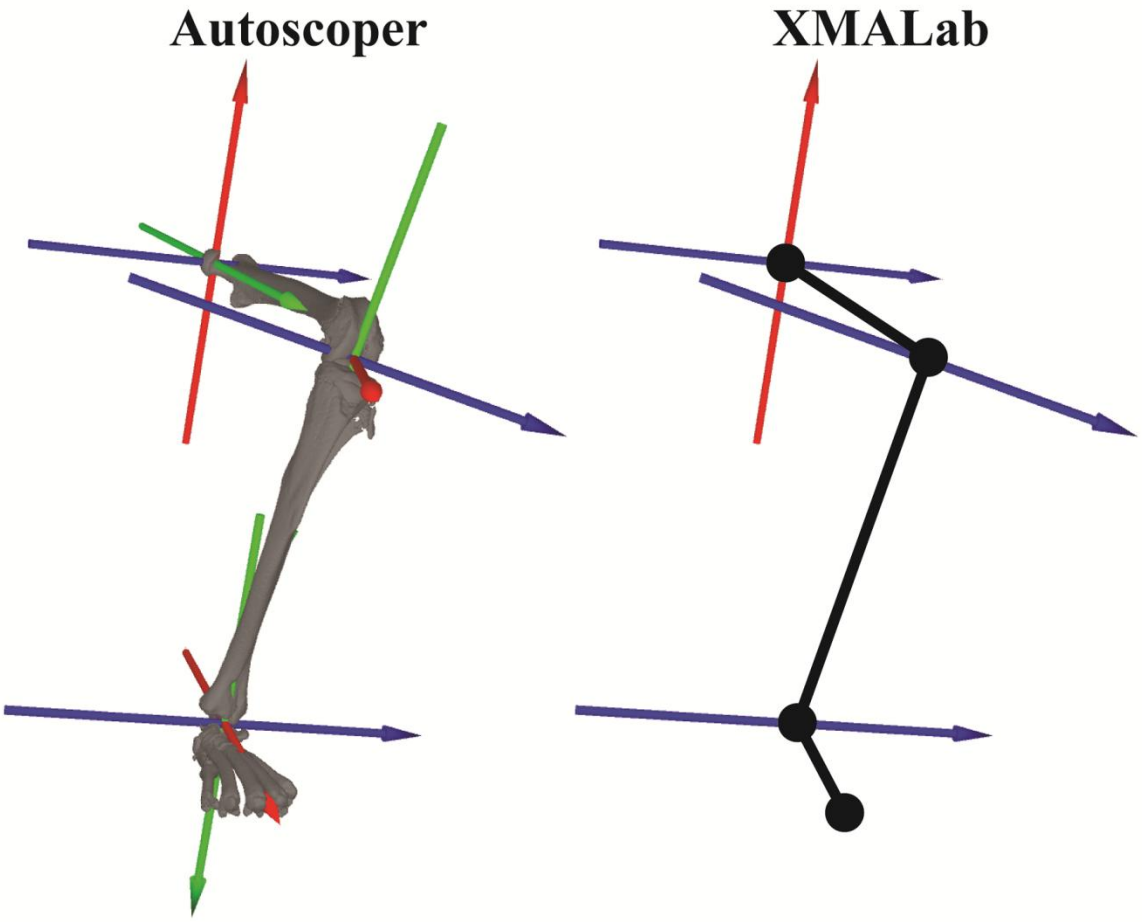

Figure 3.3: Axes of rotation that the Autoscoper and XMALab techniques recognize. Autoscoper recognizes three degrees of rotation at each joint (nine total), whereas XMALab recognizes four total degrees of rotation

Once the angles were quantified using each technique, a repeated measures t-test was performed between the XMALab and Autoscoper values at each gait cycle event for the four angles in common with both techniques: hip abduction and adduction, hip flexion and extension, knee flexion and extension, and ankle plantar flexion and dorsiflexion. For all cases α=0.05 was used and all statistical analyses were performed in SPSS software.

3.3 Results

The absolute differences, or residuals, between the XMALab and Autoscoper values were calculated for all conditions. The residuals for the four angles were then graphed and organized by gait cycle event. These graphs can be found in Appendix B. Residuals where the difference between the XMALab and Autoscoper values was significant are indicated by asterisks. Figure B.1 is displayed below.

In terms of joint rotations, ankle plantar flexion and dorsiflexion generated the largest amount of significant residuals at 3, being present at each gait cycle event. Hip abduction and adduction followed up at 2 significant residuals, while knee flexion and extension only had 1. There were no significant residuals for hip flexion and extension. In terms of gait cycle event, the most significant residuals were found at midstance (3), followed by toe off (2) and initial contact (1). All mean residuals for all angles were less than 4°.

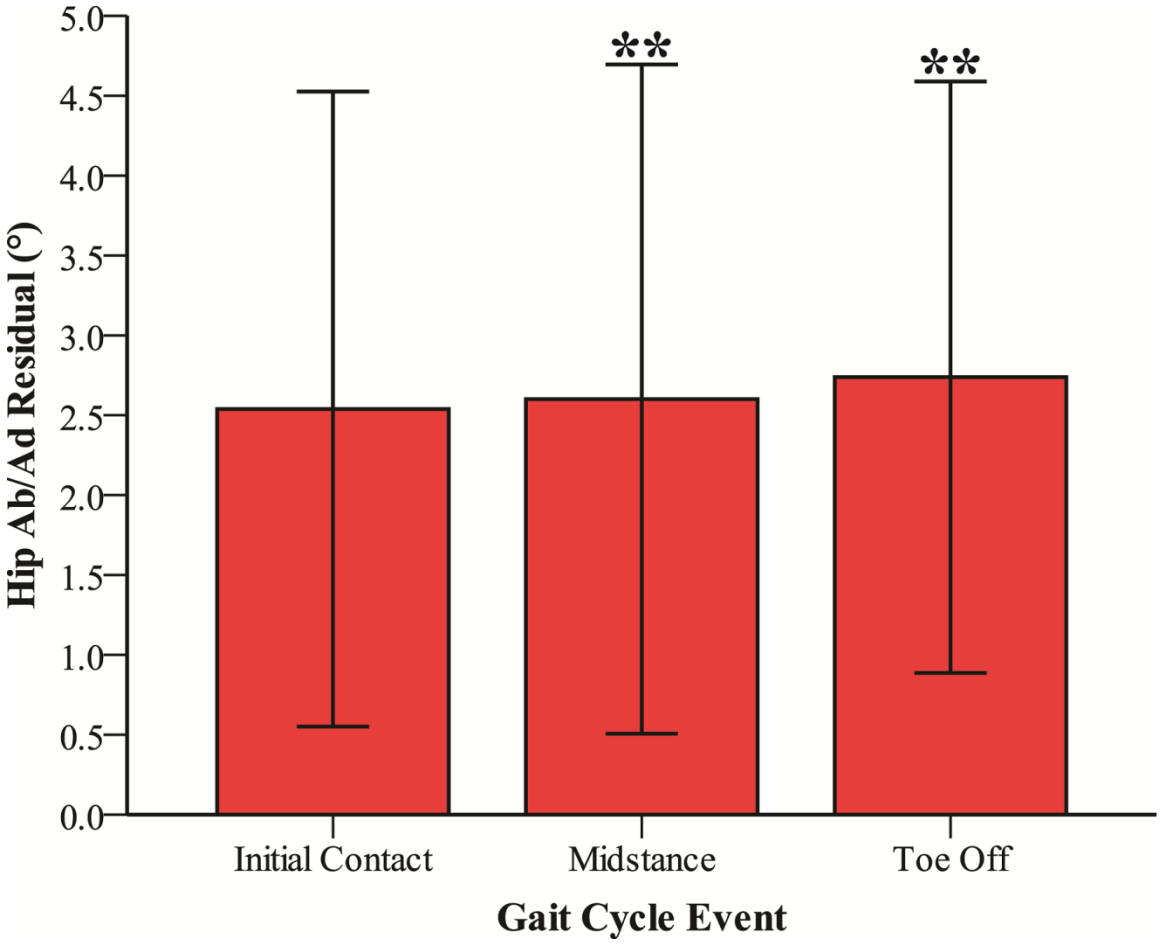

Figure B.1: Hip abduction residuals (mean ± SD) between XMALab and Autoscoper; significance indicates a significant residual between XMALab and Autoscoper, * = p < 0.10, ** = p < 0.05

3.4 Discussion

The qualitative differences between the XMALab workflow and the Autoscoper workflow have been detailed and listed. On output, XMALab is able to measure 4 anatomical angles while Autoscoper is able to measure 9 anatomical angles. Of the 9 angles Autoscoper can measure, one is the knee varus and valgus rotation. Knee varus rotation is a kinematic identifier of knee OA in humans (Chapter 1), which gives Autoscoper an advantage over XMALab for choice in an OA study. On tracking,

XMALab relies on manual recognition of joint centers while Autoscoper relies on positioning and orienting a 3D object using anatomical landmarks as guides. The subject-specific nature of Autoscoper is more objective than the approximating nature of XMALab's method. On processing time, XMALab is relatively quick while Autoscoper is relatively slow. Using broad estimates, the Autoscoper method takes roughly 5 to 6 times as long to process data as the XMALab method. On user precision error, from Table 2.2, XMALab generally has a better precision compared to the Autoscoper equivalents. While Autoscoper can measure more angles, XMALab can generally measure the fewer it has more precisely. On software requirements, the XMALab workflow can be completed using all free software while the Autoscoper workflow requires software that can have yearly subscription fees. In the scope of this thesis, all fees were circumvented using free academic subscription licenses so software requirements are not taken into account.

The quantitative differences between the XMALab workflow and the Autoscoper workflow have been computed and compiled in Figures B.1 – B.4 in Appendix B. The bar graphs show the absolute differences, or residuals, between the values calculated with XMALab and the values calculated with Autoscoper. It can be observed that even though all the residuals are similar, some gait cycle events have a significant residual whereas others do not. Significant residuals in these figures indicate that at this particular gait cycle event for this angle, the precision in both tracking methods was high enough that the difference between them (the residual) was significant. The rat's position and orientation at given gait cycle events could be a factor in why significance is found at certain times. No significant differences were found between any gait cycle events,

indicating the differences between the methods were fairly consistent. The ankle plantar flexion and dorsiflexion residual had significant differences at every gait cycle event, indicating both methods measured the angle precisely enough such that the roughly 3° residuals were significant. Conversely, the hip flexion and extension residual had no significant differences, indicating both methods measured the angle in a way such that the roughly 2.5° residuals were not significant.

When considering both the XMALab tracking method and the Autoscoper tracking method, one needed to be selected for the rat OA study. XMALab, while much quicker to process than Autoscoper and having a generally higher user precision, does not measure the knee varus and valgus rotation that is an identifying characteristic of knee OA in humans. Additionally, the objective nature of Autoscoper's tracking method (using anatomical landmarks) as opposed to the subjective nature of XMALab's tracking method (approximating joint centers) lends more repeatability to the Autoscoper method. The kinematic differences of XMALab from Autoscoper show they are not interchangeable without losing a significant amount of accuracy in some cases. For these reasons, the Autoscoper tracking method was employed in the rat knee OA study.

CHAPTER 4

ANALYSIS OF THE EFFECTS OF TWO DIFFERENT REHABILITATION INTERVENTIONS FOR KNEE OSTEOARTHRITIS ON RAT HIND LIMB JOINT KINEMATICS

4.1 Introduction

In Chapter 2, the custom high-speed biplanar videoradiography system was described and two workflows were defined. The system's accuracy and precision were measured with a validation study using four phantoms of know length over 1800 frames of tracking each. User precision was measured to quantify how much the user can possibly affect the accuracy of tracking. In Chapter 3, the two workflows were described in detail and compared. Motion data was used to quantify residuals between the two methods and significant residuals were identified with a repeated measures t-test. The combination of the qualitative comparison and the quantitative differences resulted in choosing the Autoscoper tracking method for the rat knee OA study.

As discussed in Chapter 1, the rat MMT model has been used to study human knee OA interventions and results in morphological changes similar to human knee OA [8] [9]. By focusing on gait changes, the effects of interventions can be quantified and measured. Previously, rat knee OA has been studied by measuring spatiotemporal parameters, such as stride length and limb stance time [10] [11] [17] [18]. The hind limb kinematics of rats with knee OA have been seldom measured. Boettger measured the range of motion of knee angles using a single plane X-ray system [20]. Using the system

described in Chapter 2, full rat hind limb kinematics and spatiotemporal parameters are measureable.

Regarding interventions to test, as briefly discussed in Chapter 1, repetitive loading and reduced loading are incorporated into the experimental design. Repetitive loading will be induced by elevated levels of exercise in the rats. To test this intervention, rats will experience specific levels of exercise to see if the regimen alleviates the OA or aggravates the OA. Kinematic and spatiotemporal results will be utilized to determine the severity of OA. Reduced loading will be induced by immobilization of the rat hind limb. The goal of this intervention is to measure if the lack of weight on the hind limb exacerbates or stalls the knee OA.

4.2 Methodology

14 male Lewis rats (304 ± 57 g) were selected for MMT surgery in their left hind limbs. The rats were randomly assigned to one of four groups: the sham surgery group (n = 4, SHAM), the non-intervention group (n = 3, NON), the running intervention group (n = 3, RUN), or the immobilization intervention group (n = 4, IMB). As described by Bendele, the MMT surgery consists of a transection of the MCL and cutting the meniscus at its narrowest point [8]. The SHAM group, designed as a control for the surgery, received the MCL cut but not the meniscus cut. The other three groups, NON, RUN, and IMB, underwent the full surgery. Prior to surgery, all rats participated in 4 week treadmill training. After surgery, rats were given one week of recovery time before being assigned to a group. The SHAM and NON groups were acclimated over time to pre-injury treadmill running speeds. The RUN group underwent an exercise regimen of 30 minutes per day, 4 days per week at a speed of 0.2 m/s. The IMB group was immobilized by

shaving the lower torso and left hind limb and wrapping the limb with elastic tape such that the hip was flexed and the knee and ankle were extended. The immobilization was replaced as needed and only removed for X-ray data collection.

For data collection, the left hind limb kinematics at three gait cycle events were investigated: initial contact, midstance, and toe off. Data collection was performed at 8 weeks post-surgery. For collection, rats were enclosed in a 21.5 x 15.0 x 56.0 cm Plexiglas treadmill oriented skew sagittal to the two X-ray emitters of the system. Rats walked on the treadmill at 0.5 m/s while X-ray videos were taken during periods of consistent locomotion. Five stance cycles of steady locomotion were identified for each rat. A mild shock stimulus and a brush were placed at the back end of the treadmill to encourage locomotion. X-rays were emitted from the two X-ray emitters at 42 kv and 80 mA and captured with the IIs and high-speed digital video cameras. One hundred X-ray images per second per camera were captured, with the duration of exposure not exceeding 6 seconds. All videos were saved to a dedicated computer. Pictures of the undistortion grids and calibration object were also taken. After collection, rats were euthanized and CT scans were taken of the left hind limb using EPIC-μCT at 100 μm resolution. All data were collected according to a protocol approved by the Georgia Institute of Technology IACUC. Figure 4.1 depicts the X-ray video data collection procedure.

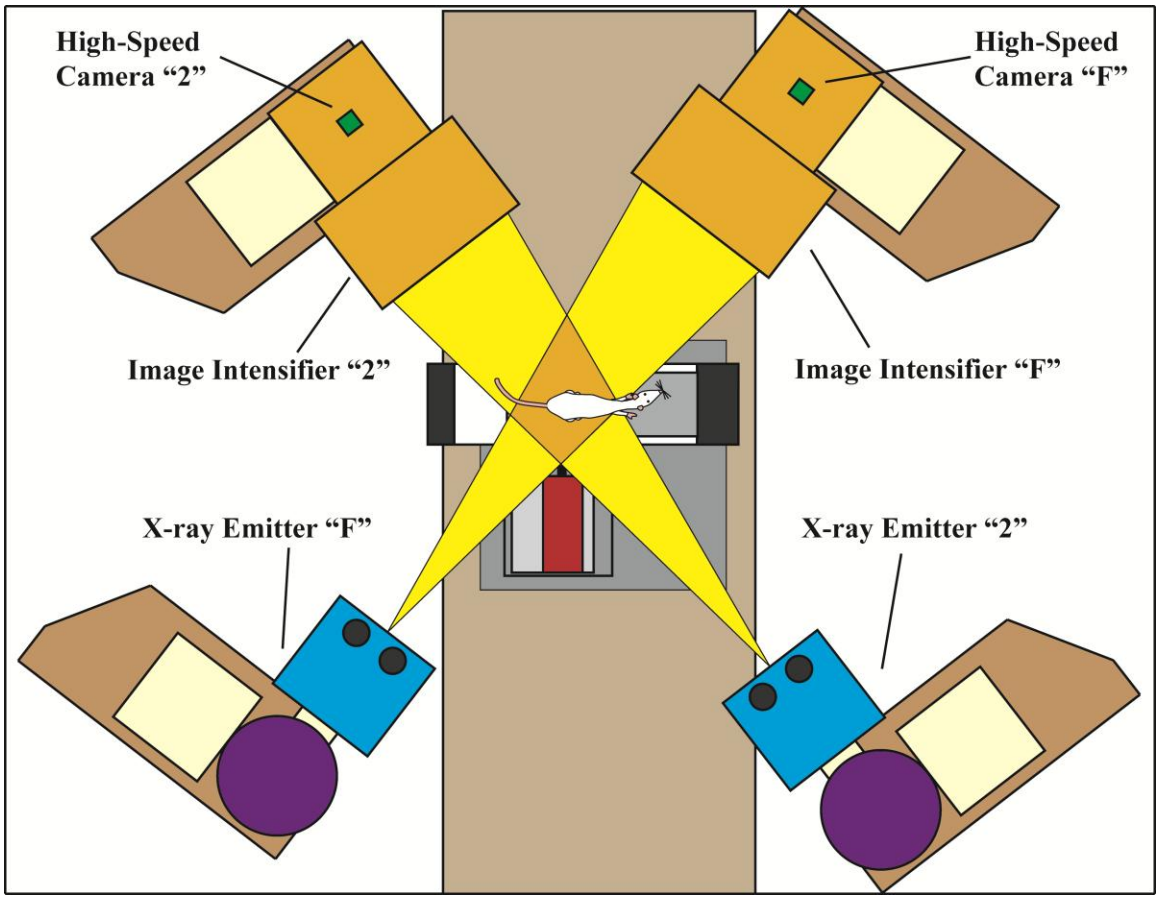

Figure 4.1: Diagram of the custom biplanar high-speed videoradiography system during data collection, with a rat's hind limbs in the imaging volume

After collection, distortion correction was applied to the X-ray videos using the undistortion grid images (as discussed in Chapter 2). The imaging volume was then calibrated using the images of the calibration object (also discussed in Chapter 2), producing calibration matrices allowing for accurate three-dimensional positioning. 3D bone surface models and DRRs were manually segmented out of the CT scans for the femur, tibia and fibula, and foot then formatted to the correct specifications. The DRRs, calibration matrices, and undistorted X-ray videos were then imported into Autoscoper. Bone DRRs were manually oriented in three dimensions in Autoscoper and saved as a

key frame. This was repeated for the three gait cycle events (initial contact, midstance, and toe off) for all five identified stance cycles for all 14 rats for a total of 210 key frames. Spatiotemporal parameters were also measured. In XMALab, the positions of the MTP joint for both the injured and the non-injured legs were tracked. This information was then used to calculate stride length and time, step lengths and times, temporal and spatial symmetry, etc., as described by Kloefkorn [11].

Using the calibration matrices, a 3D environment was created in Maya. The 3D bone surface models were used to create JCSs, as described in Chapter 3. The DRR tracking data exported from Autoscoper were then applied to the 3D bone surface models. The accuracy of the orientations was verified by importing the X-ray videos into the 3D environment and visually checking for agreement. The JCSs were updated with the imported orientations and joint angles were exported. As they are defined, the joint angles are the rotations of the distal body relative to the proximal body, with reference to the "zero poses". The hip angles are the exception, being defined as the femur JCS relative to the calibrated "vertical" vector and the treadmill's "forward" vector.

After the data were exported and organized, statistical analyses were performed using SPSS software. Because group interactions were being analyzed, ANOVA tests were performed. Before running the tests, a conservative approach was used to check if the data was parametric or non-parametric. A Shapiro-Wilks test for normality and a Levene's test for homogeneity of variances were performed for all groups at all gait cycle events. Groups that were statistically normal and did not exhibit a significant difference in variances were tested using an ANOVA with a Tukey HSD post-hoc test for statistical significance. Groups that were not normal or exhibited a significant difference in

variances were analyzed using non-parametric equivalents: the Kruskal-Wallis group test and the Mann-Whitney test. For significance, α=0.05 was used for all tests.

4.3 Results

All analyzed stance cycles were classified according to Hildebrand based on their corresponding gait cycles [33]. Each gait cycle was consistently found to be a walking gait with greater than 50% duty factor on the hindlimb of interest. Across the groups, there was some variability between trotting and lateral sequence footfall patterns for the walking gait. The RUN group generally walked with a trotting footfall pattern while the other groups generally walked with a lateral sequence footfall pattern [33].

The nine angles measurable by Autoscoper, hip abduction and adduction, internal and external hip rotations, hip flexion and extension, knee varus and valgus rotations, internal and external knee rotations, knee flexion and extension, ankle inversion and eversion, internal and external ankle rotations, and ankle plantar flexion and dorsiflexion, were measured and graphed at three gait cycle events, initial contact, midstance, and toe off. These graphs are collected in Appendix C. Significant differences between groups are indicated by asterisks. Two asterisks indicate significance levels of $p < 0.05$, while one asterisk indicates significance levels of $p < 0.10$. These two levels are included to indicate what the data show and what they are trending towards. Several graphs were selected and copied in this section. Figures C.1, C.4, C.6, and C.9 are shown below.

Hip abduction (Figure C.1) shows a significant difference between the SHAM group and the other groups at midstance. Similarly, the IMB group is significantly more abducted than the other groups at midstance. At toe off, a lower level of significance

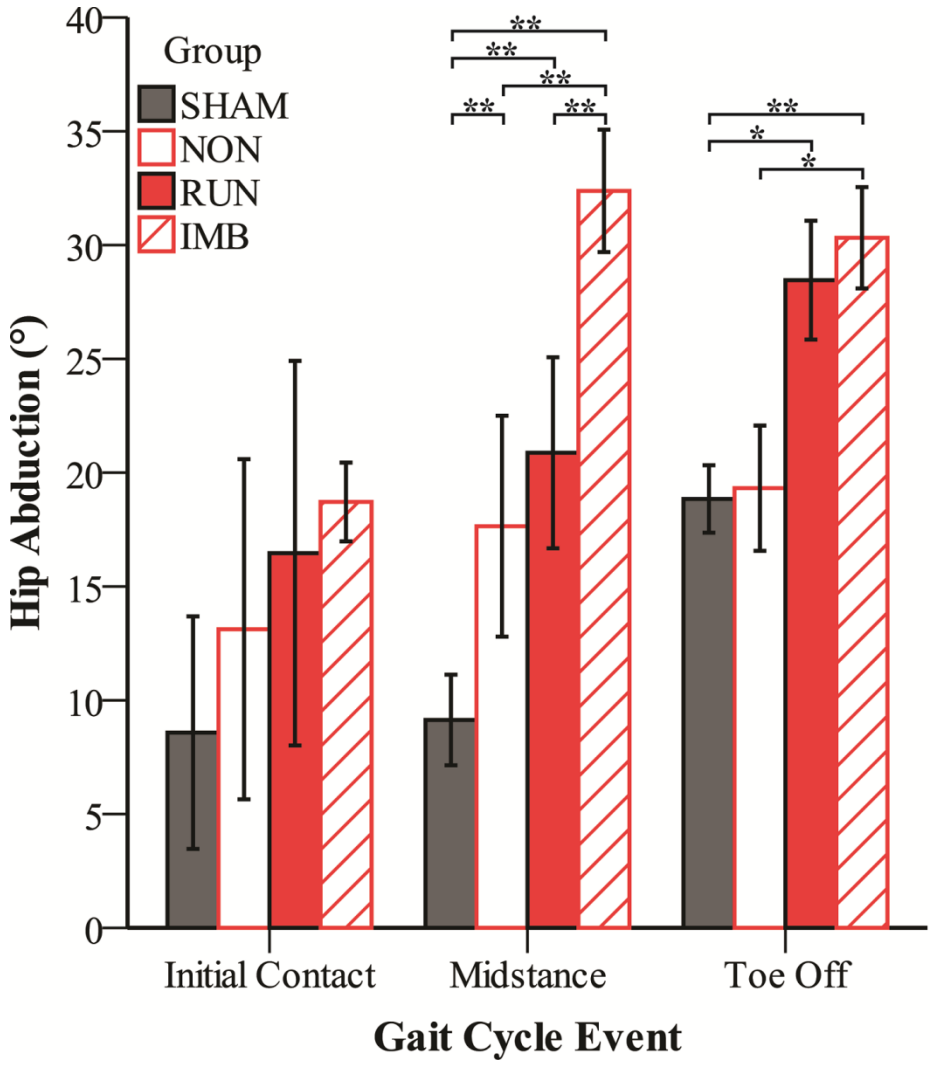

Figure C.1: Hip abduction (mean ± SD) quantified using Autoscoper. * = p < 0.10, ** = p < 0.05. 0° indicates the femur pointing forward

shows the RUN and IMB groups being more abducted than the SHAM and NON groups. Hip external and internal rotations (Figure C.2) show the IMB group being significantly more internally rotated than the other groups at midstance, and a lower level of significance at initial contact between most of the groups. Hip flexion and extension (Figure C.3) show that at initial contact, the IMB group was more extended than the SHAM and NON groups.

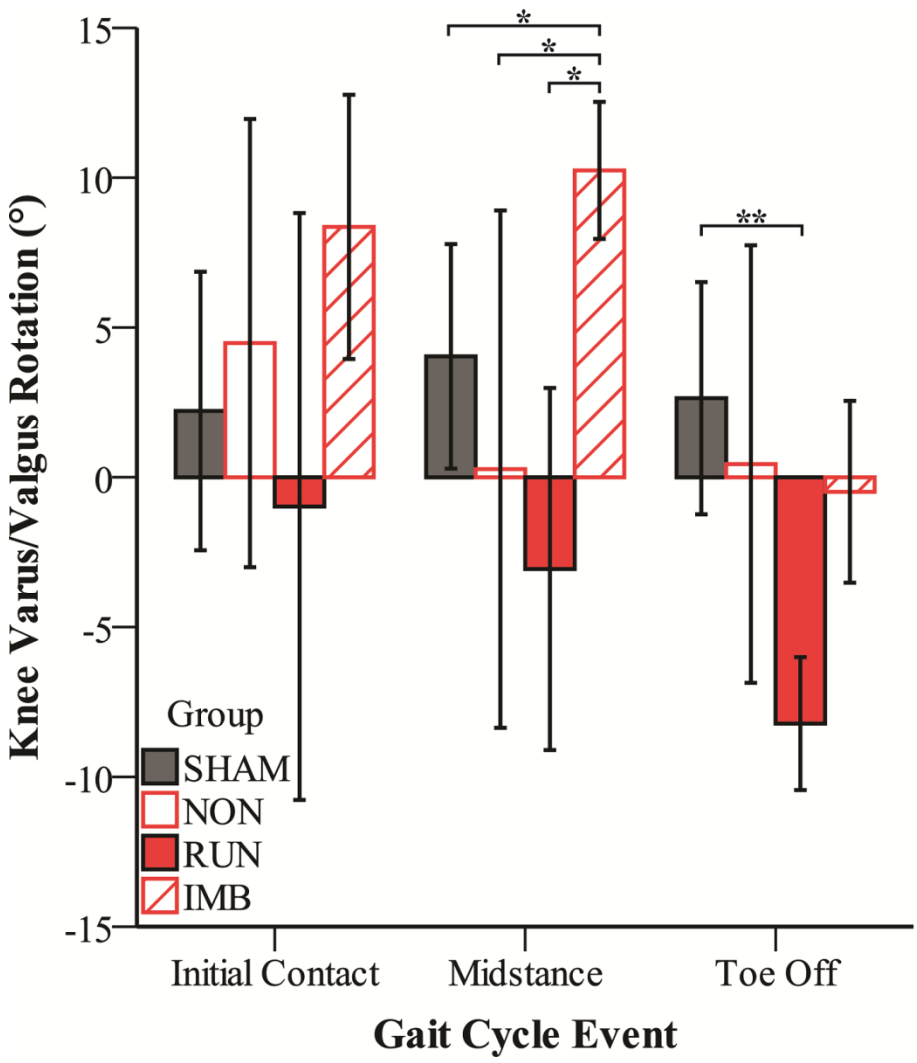

Figure C.4: Knee varus/valgus rotation (mean ± SD) quantified using Autoscoper. * = p < 0.10, ** = p < 0.05. 0° indicates no varus or valgus rotations

Knee varus and valgus rotations (Figure C.4) show that at midstance the IMB group has more valgus rotation than the other groups (low significance), and that at toe off the RUN group has significantly more varus rotation than the SHAM group. Knee external and internal rotations (Figure C.5) only show that at toe off, the IMB group is less internally rotated than most of the groups. Knee extension and flexion (Figure C.6) show that at initial contact, the IMB group is significantly more extended than the other

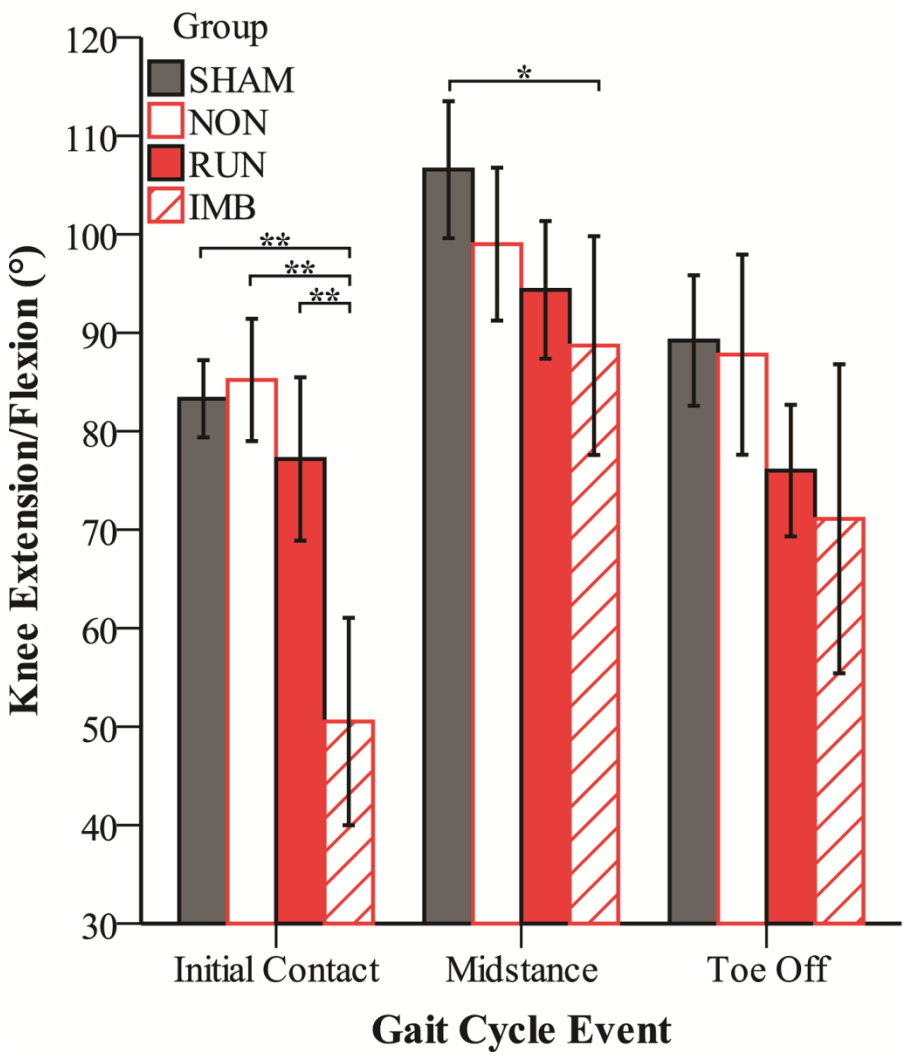

Figure C.6: Knee extension/flexion (mean ± SD) quantified using Autoscoper. * = p < 0.10, ** = p < 0.05. 0° indicates a fully extended tibia and fibula

groups. At midstance, the IMB group trends toward being less flexed than the SHAM group.

Ankle inversion and eversion (Figure C.7) is dominated by the IMB group having significantly more inversion than most of the others at all gait cycle events. Ankle external and internal rotations (Figure C.8) have no significant interactions. Ankle dorsiflexion and plantar flexion (Figure C.9) display varying levels of significance at

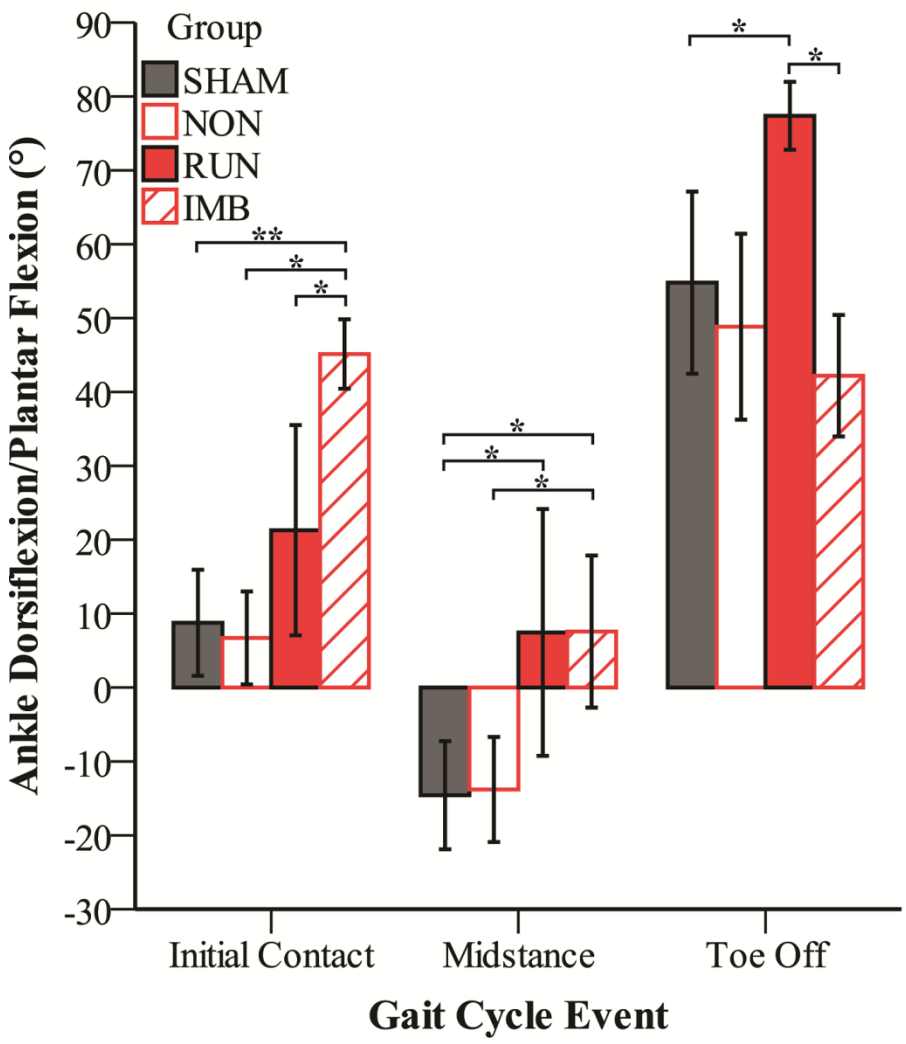

Figure C.9: Ankle dorsiflexion/plantar flexion (mean ± SD) quantified using Autoscoper. * = p < 0.10, ** = p < 0.05. 0° indicates the foot is perpendicular to the tibia and fibula

initial contact with the IMB group being more plantar flexed than the rest. At midstance, the SHAM and NON groups show reduced significance in being more dorsiflexed than the RUN group. At toe off, the RUN group has reduced significance with higher plantar flexion than the SHAM and IMB groups.

As mentioned earlier, spatiotemporal parameters were measured along with the kinematics. Nine parameters were calculated for both the OA leg and the contralateral

leg: limb stance time, limb stride time, percentage stance time (also called duty factor), single limb support, temporal symmetry, step length, step width, stride length, and spatial symmetry. These parameters were calculated based on the equations described by Kloefkorn et al. [11]. The parameters were graphed and collected in Appendix C after the kinematic results. Significance levels are indicated with asterisks as before. Several graphs were selected and copied below. Figures C.12, C.13, and C.17 are shown below.

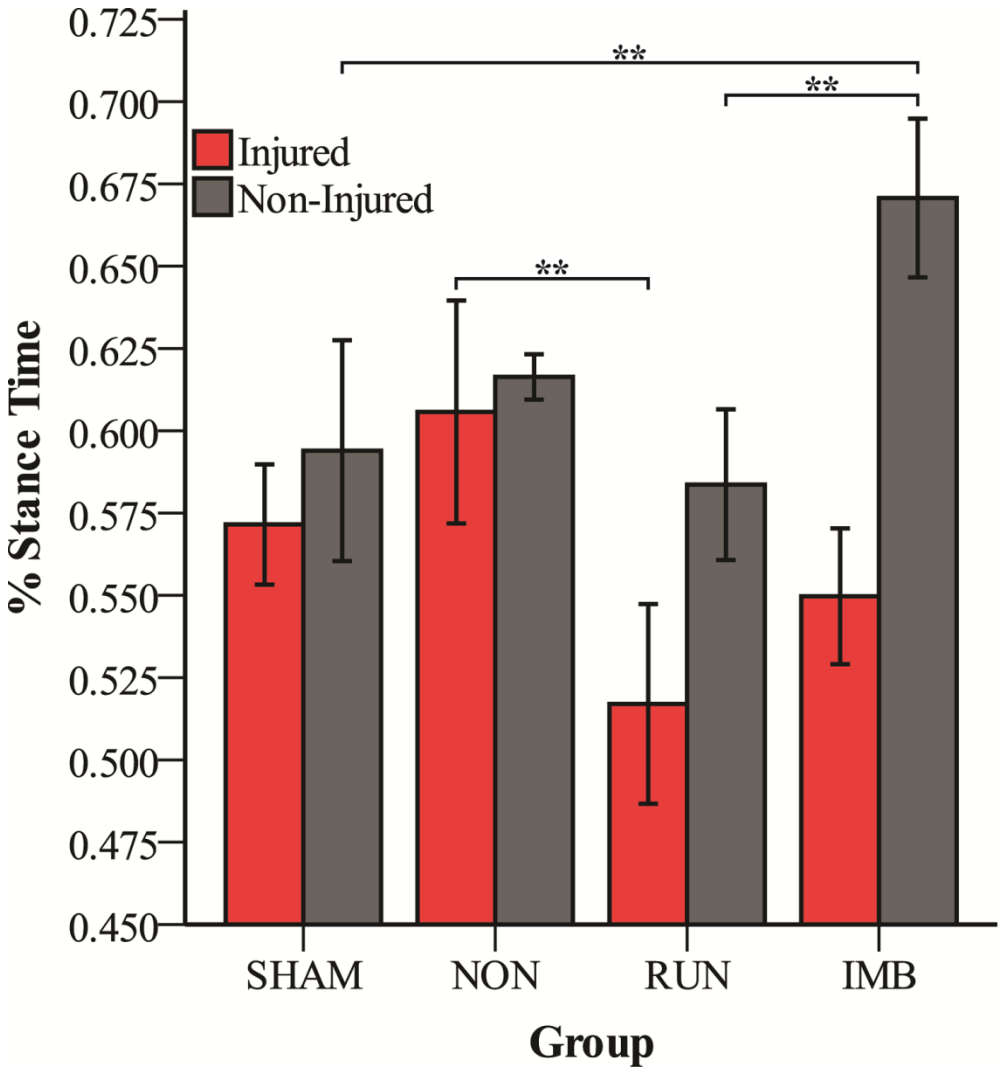

Figure C.12: Percentage stance time (mean ± SD) for both the injured (left) and non-injured (right) legs. * = p < 0.10, ** = p < 0.05. Values indicate amount of time the limb is in contact with the ground as a percentage of the stride time

Limb stance time (Figure C.10) and limb stride time (Figure C.11) show no significant differences between groups. Percentage stance time (Figure C.12) shows the RUN injured limbs have a lower percentage than the NON group, and the IMB group's non-injured limb has a higher percentage than most of the groups. Single limb support (Figure C.13) shows the RUN group's non-injured limb has a higher single limb support

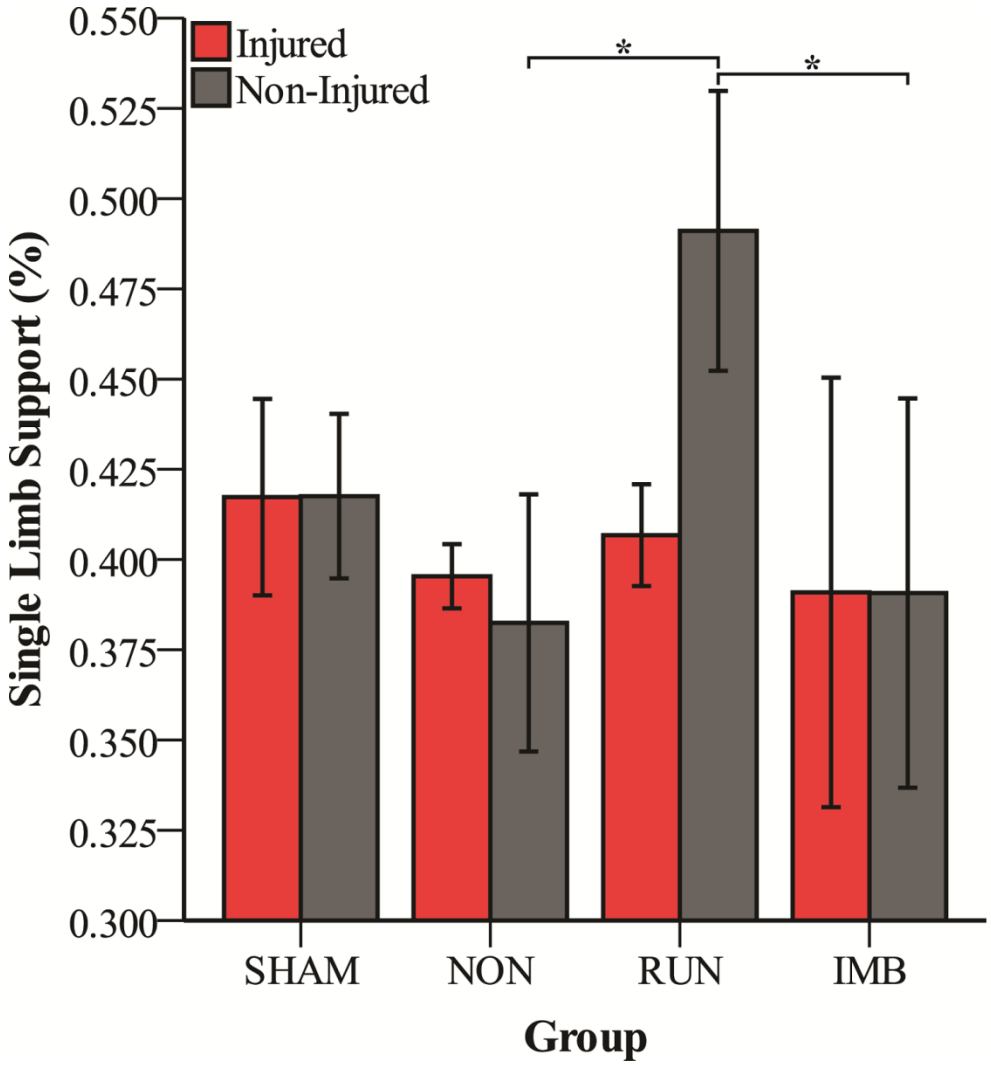

Figure C.13: Single limb support (mean ± SD) for both the injured (left) and non-injured (right) legs. * = p < 0.10, ** = p < 0.05. Values indicate amount of time the limb is in contact with the ground while the contralateral limb is not, as a percentage of stride time

percentage than most of the other groups, at a lower significance. Step length (Figure C.14) shows that for the IMB group, the injured to non-injured step (left to right) covered significantly less distance than most of the groups. Conversely, step width (Figure C.15) shows that the IMB group, for both step types, has a generally significantly wider step than the other groups. A low interaction is also shown in the RUN injured to non-injured steps (left to right) being slightly wider than the SHAM steps. Similar to the step

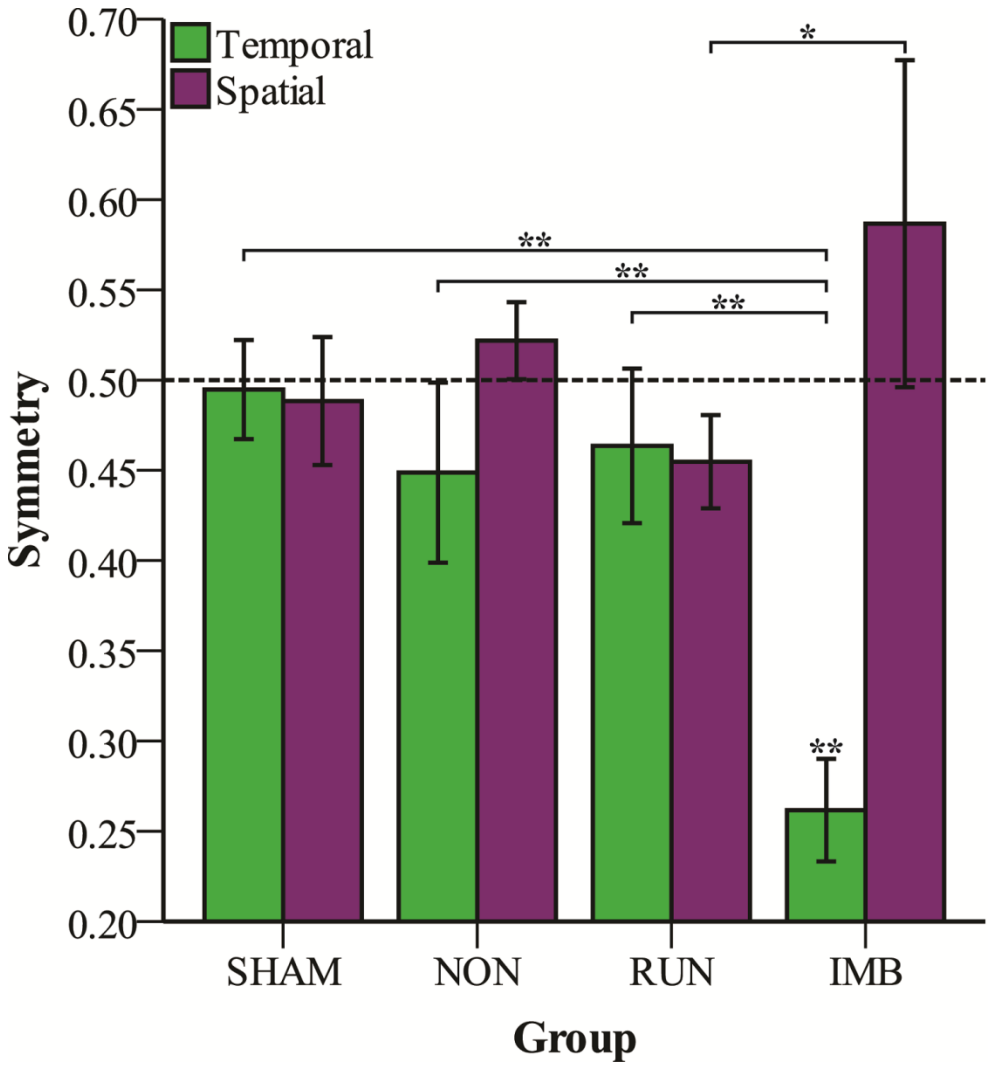

Figure C.17: Gait symmetry (mean ± SD) both spatially and temporally. Symmetry values of 0.50 indicate the right foot initial contact occurs exactly halfway through a left foot stride, in length or time respectively. * = p < 0.10, ** = p < 0.05

lengths, the stride lengths (Figure C.16) show the IMB group having generally significantly smaller stride lengths than the other groups. Temporal and spatial symmetry are grouped together in Figure C.17. With temporal symmetry, the IMB group has a significantly lower symmetry than the other groups, and is the only group to have a symmetry significantly different than 0.50 (balanced symmetry). With spatial symmetry, the IMB group has a low significance difference with the RUN group.

4.4 Discussion

The kinematics and spatiotemporal parameters for 14 rats organized into four experimental groups were measured at three gait cycle events. Nine joint angles and nine spatiotemporal parameters were quantified and statistically compared across groups. Generally, few significant differences were found at initial contact. This could be due to full weight not having been applied on the limb yet. The interactions between groups are discussed below.

The SHAM group acted as a control for the MMT procedure while the NON group acted as a control for the tested interventions. The NON group appeared to have developed a mild degree of knee OA. This was evident through increased hip abduction at midstance compared to the SHAM group. This was not present through to toe off, leading to the appearance of only slight OA. The RUN group, while tested as an intervention, appeared to have developed more advanced knee OA. This was seen in increased hip abduction at midstance and toe off (compared to SHAM) and in a varus rotation of the knee found at toe off. Recalling Chapter 1, a knee varus rotation is a kinematic presentation of knee OA in humans. In addition, the RUN group developed some ankle compensations causing it to have a more plantar-flexed ankle at midstance

and toe off (albeit with reduced significance). With the hip more abducted in the RUN group, the slightly wider step width (relative to SHAM) appeared to follow logically. Between the NON and RUN groups, comparisons of mild and advanced knee OA can be made. As knee OA advanced across groups, injured limb percentage stance time decreases and contralateral limb single limb support increases. These results indicate rats with advanced knee OA spend less time on their injured limb during gait.

The IMB group yielded kinematic and spatiotemporal results significantly different from the other groups in many aspects. To describe in general terms, at initial contact, the average IMB group: hip was more extended and internally rotated than the other groups; knee was more extended than the other groups; ankle was more inverted and planter flexed than the other groups. At midstance, the average IMB group: hip was more abducted and internally rotated than the others; knee was generally less extended and more valgus rotated; ankle was more inverted and slightly more plantar flexed. At toe off, the average IMB group: hip was more abducted; knee was more externally rotated; ankle was more inverted. All the while these kinematic observations were made the gait was shown to be significantly asymmetric (temporally) with a significantly wider and shorter step and a smaller stride. Based on these results, it is difficult to determine if the gait changes were due to knee OA or atrophic changes from limb disuse during immobilization, as discussed by Ando [13].

CHAPTER 5

CONCLUSIONS

The rat MMT model of knee OA was used to test two rehabilitation interventions: an exercise and an immobilization intervention. To measure the effects of these interventions on gait, a custom biplanar high-speed videoradiography system was utilized. Before using the system extensively, workflows were developed and a validation study was performed to measure its accuracy and precision. Two workflows, the XMALab method and the Autoscoper method, were tested and developed. A validation study using four phantoms of known lengths was run, yielding a system accuracy of 0.087 mm and a precision of 0.073 mm. User precision values were also measured to account for any variability in measurements. Between the two workflows developed, the Autoscoper method was chosen for use in the rat knee OA study due to its ability to measure more angles. With the system defined and a workflow decided, the rat knee OA rehabilitative interventions were tested. Fourteen rats were randomly sorted into 4 groups: non-intervention, exercise intervention, immobilization intervention, and sham surgery. Using Autoscoper, hind limb 3D kinematics and gait spatiotemporal parameters were measured at initial contact, midstance, and toe off. The non-intervention group was found to have developed mild knee OA while the exercise intervention group developed advanced knee OA with the presence of a knee varus rotation, similar to human knee OA. The immobilization intervention group was significantly different from the rest and the results could not be distinguished from possible atrophic changes.

Upon completing this study, several recommendations were realized. The angle between the X-ray emitters can be optimized further. Due to the fact that the workflows were being developed in parallel with data collection for this thesis, the angle between the X-ray emitters was not optimized for these data. An X-ray angle closer to perpendicular would be more efficient. Having a more perpendicular X-ray angle would allow for easier tracking in Autoscoper, as the X-ray videos would have greater differences between them. This in turn would potentially speed up the process of DRR tracking and reduce the total processing time. Care would have to be taken with the less obtuse angle to make sure the X-ray images would not be obscured by any part of the treadmill assembly. The calibration object's precision can be optimized as well. Since this thesis' data collection, a paper from Knorlein has been published detailing an easy-to-assemble calibration cube made from LEGO bricks [26]. This new calibration cube would be a suitable replacement to the crafted calibration object used in this thesis and could potentially increase accuracy in the imaging volume. Regarding tracking, if the lack of implanted markers in the experimental subjects is not crucial it is highly recommended to implant three radio-opaque markers into each bone around a joint of interest. Three implanted markers in each bone would allow for motion tracking in XMALab. Using the automated registration and point detection algorithms included in the software, marker tracking's difficulty would be trivialized. This would allow for easier motion tracking at more than three gait cycle events and possibly tracking motion during the entire gait cycle. Three markers would be a minimum amount needed and any more would help with precision [23].

This innovative study appears to be the first to measure full 3D hind limb kinematics in a rat model of knee OA. The ability to measure angles that cannot be entirely found in the sagittal plane with a single plane X-ray system shows promise for the future of biplanar videoradiography. By measuring kinematic changes in a rat with advanced knee OA, parallels can be drawn between human knee OA gait changes and rat knee OA gait changes with a common measure of knee varus rotations. With a larger treadmill, the techniques applied in this thesis can be applied to larger animals, such as rabbits or cats, and a variety of pathologies that affect gait can be studied and analyzed.

APPENDIX A

ACCURACY AND PRECISION DATA

Table A.1: System Validation – Accuracy and Precision

Phantom	Material	Distance (mm)	Accuracy Mean (mm)	Precision S.D. (mm)	Number of Frames	Set Velocity (mm/s)	Measured Velocity (mm/s)	Precision S.D. (mm/s)	Marker 1 (Front) Reprojection Error (pixels)	Marker 2 (Back) Reprojection Error (pixels)
L1	Lego	16.0	16.093	0.058	600	38.333	6.398	3.186	0.140318±0.116973	0.189231±0.117573
			16.131	0.047	600	43.333	8.980	3.301	0.638841±0.241495	0.45103±0.233663
			16.090	0.069	600	50.000	19.008	5.366	0.380114±0.298907	0.35872±0.235948
L2	Lego	32.0	31.982	0.049	600	38.333	6.307	3.158	0.431039±0.249151	0.163612±0.121457
			31.966	0.063	600	43.333	9.568	3.409	0.265569±0.200578	0.246195±0.154677
			31.924	0.103	599	50.000	17.879	4.847	0.306301±0.21379	0.266279±0.180107
L3	Lego	64.0	63.910	0.050	600	38.333	5.488	2.488	0.638647±0.255132	0.16822±0.109579
			63.869	0.112	600	43.333	12.543	3.968	0.460399±0.36934	0.257942±0.154222
			63.882	0.135	600	50.000	15.998	4.802	0.610842±0.456953	0.20325±0.136973
M	Polypropylene	38.1	38.334	0.051	600	38.333	7.398	2.931	0.26474±0.20443	0.641904±0.25431
			38.336	0.053	600	43.333	10.948	3.564	0.321471±0.230722	0.755073±0.27717
			38.308	0.093	600	50.000	19.572	5.491	0.565909±0.330535	0.984389±0.408921

Camera 1 Undistortion Error (pixels)	Camera 2 Undistortion Error (pixels)	Camera 1 Calibration Error (pixels)	Camera 2 Calibration Error (pixels)	Marker 1 Average Reprojection	Marker 1 Average Reprojection Precision	Average Reprojection Error (pixels)	Marker 2 Average Reprojection Precision (pixels)
0.06±0.04	0.06±0.04	0.58±0.29	0.67±0.67	0.4186825	0.2640505	0.390487083	0.198716667

Phantom	Average Accuracy Error (mm)	Average Precision (mm)
L1	0.104710949	0.058
L2	0.042354417	0.071
L3	0.112883594	0.099
M	0.226067088	0.066

Average Lego Accuracy (mm)	Average Lego Precision (mm)
0.086649653	0.076
Total Average Accuracy (mm)	**Total Average Precision (mm)**
0.121504012	0.073

Minimum Accuracy Error (mm)	Precision (mm)
0.017715793	0.047
from L2, 2.3 m/min	from L1, 2.6 m/min

Maximum Accuracy Error (mm)	Precision (mm)
0.235804916	0.135
from M, 2.6 m/min	from L3, 3.0 m/min

APPENDIX B

RESIDUALS OF ANGLE COMPARISONS BETWEEN XMALAB AND AUTOSCOPER

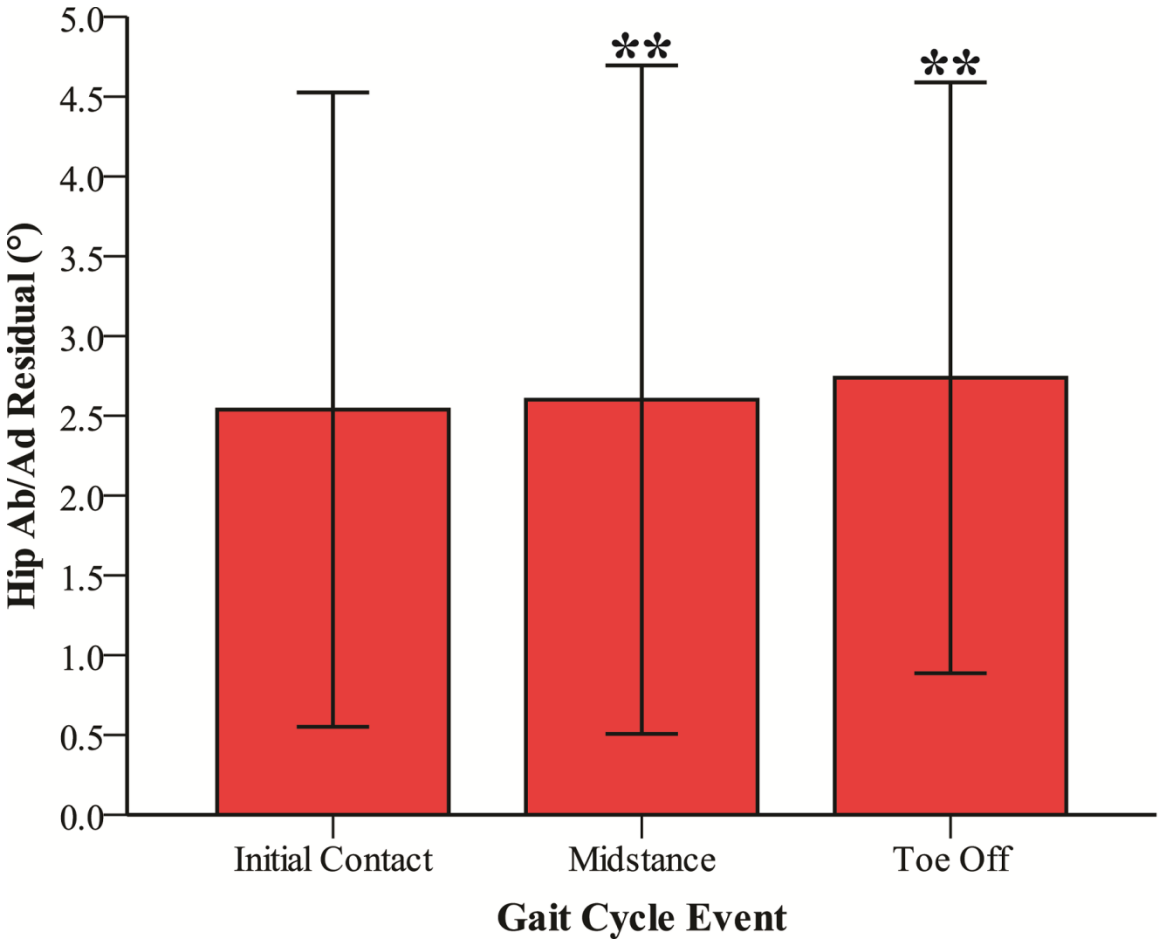

Figure B.1: Hip abduction residuals (mean ± SD) between XMALab and Autoscoper; significance indicates a significant residual between XMALab and Autoscoper, * = p < 0.10, ** = p < 0.05

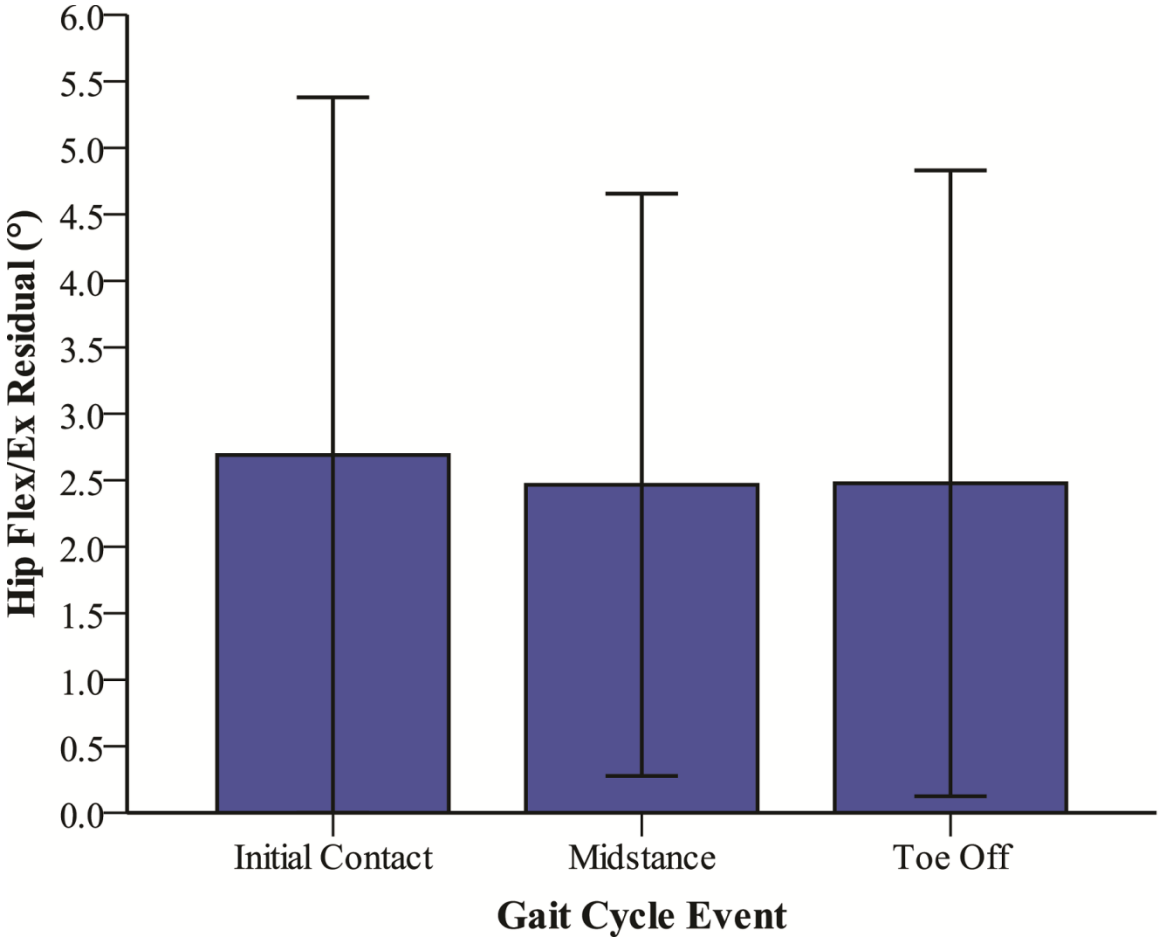

Figure B.2: Hip flexion/extension residuals (mean ± SD) between XMALab and Autoscoper; significance indicates a significant residual between XMALab and Autoscoper, * = p < 0.10, ** = p < 0.05

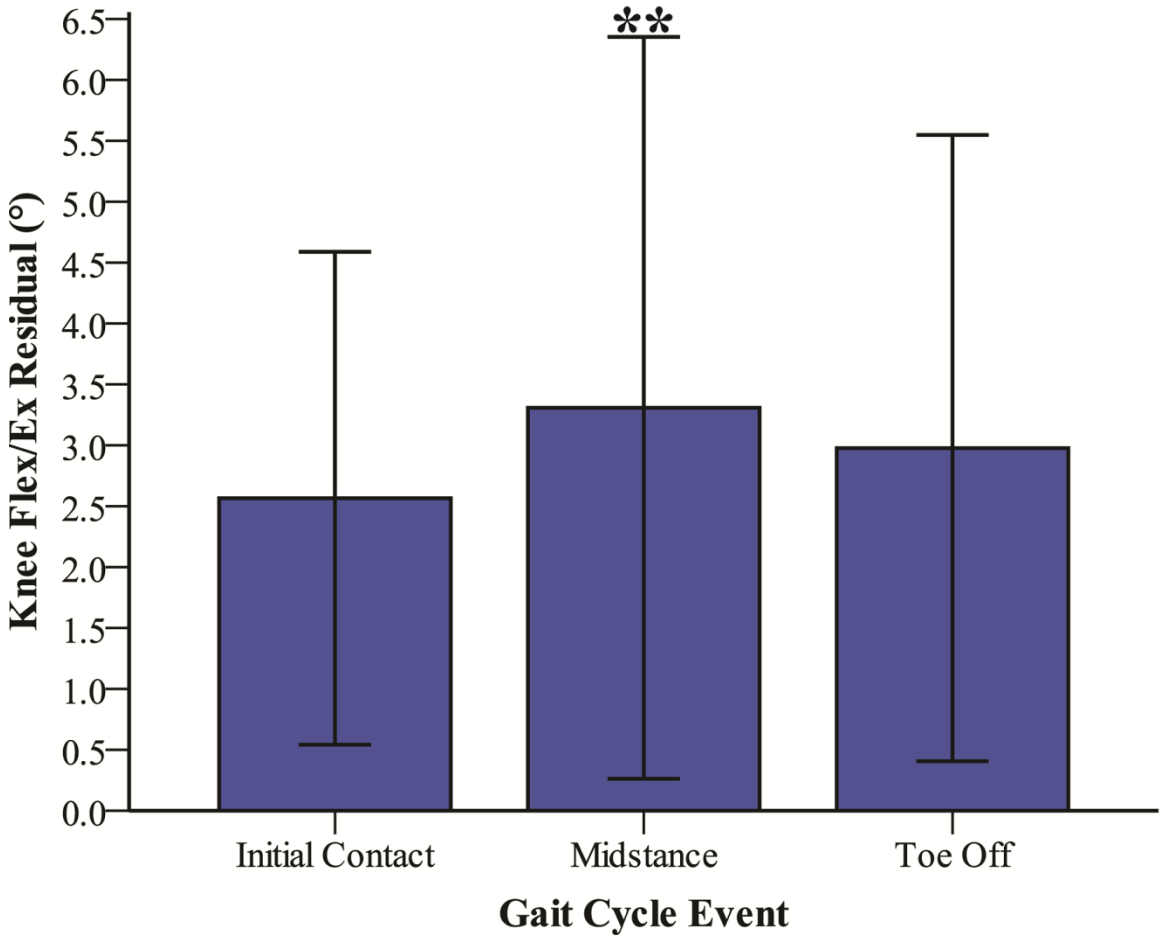

Figure B.3: Knee flexion/extension residuals (mean ± SD) between XMALab and Autoscoper; significance indicates a significant residual between XMALab and Autoscoper, * = $p < 0.10$, ** = $p < 0.05$

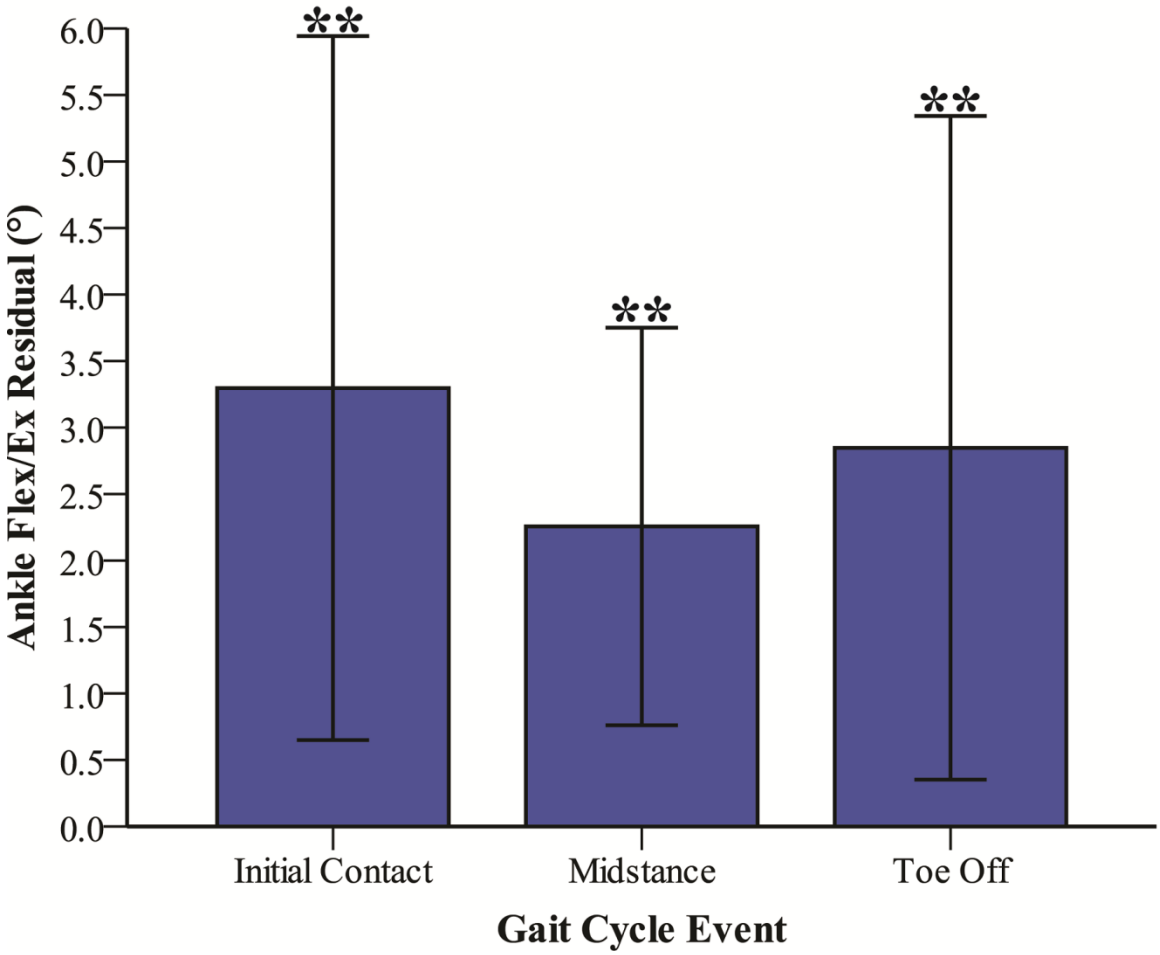

Figure B.4: Ankle dorsiflexion/plantar flexion residuals (mean ± SD) between XMALab and Autoscoper; significance indicates a significant residual between XMALab and Autoscoper, * = p < 0.10, ** = p < 0.05

APPENDIX C

RAT HIND LIMB KINEMATIC AND SPATIOTEMPORAL DATA

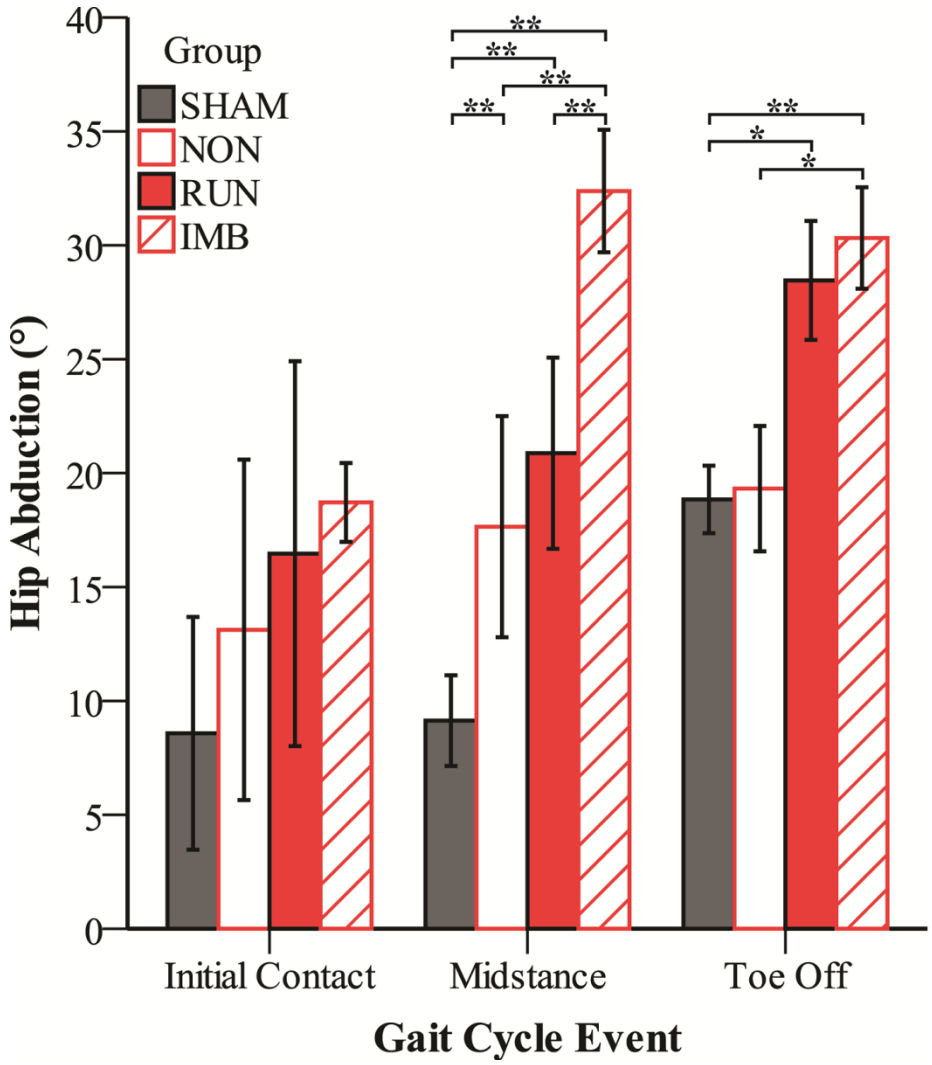

Figure C.1: Hip abduction (mean ± SD) quantified using Autoscoper. * = p < 0.10, ** = p < 0.05. 0° indicates the femur pointing forward

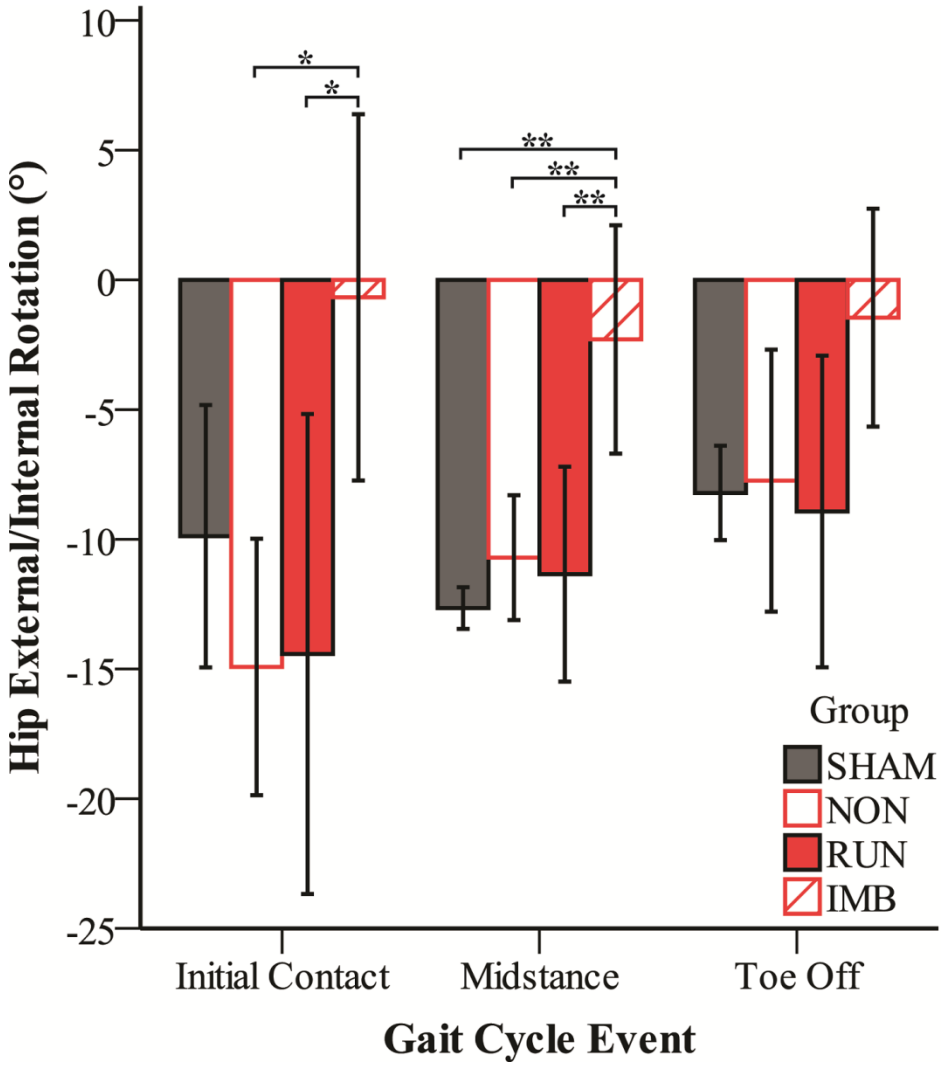

Figure C.2: Hip external/internal rotation (mean ± SD) quantified using Autoscoper. * = p < 0.10, ** = p < 0.05. 0° indicates no femoral rotation

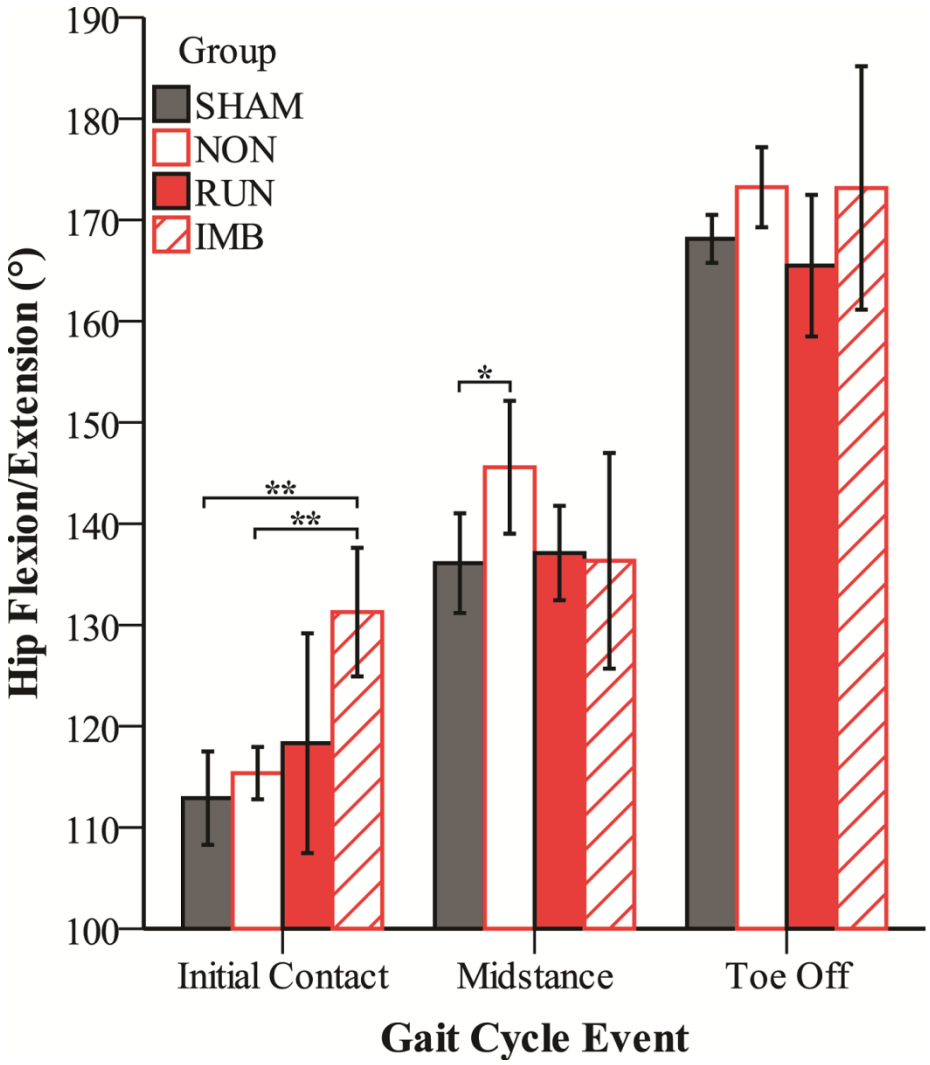

Figure C.3: Hip flexion/extension (mean ± SD) quantified using Autoscoper. * = p < 0.10, ** = p < 0.05. 90° indicates the femur being parallel with the ground

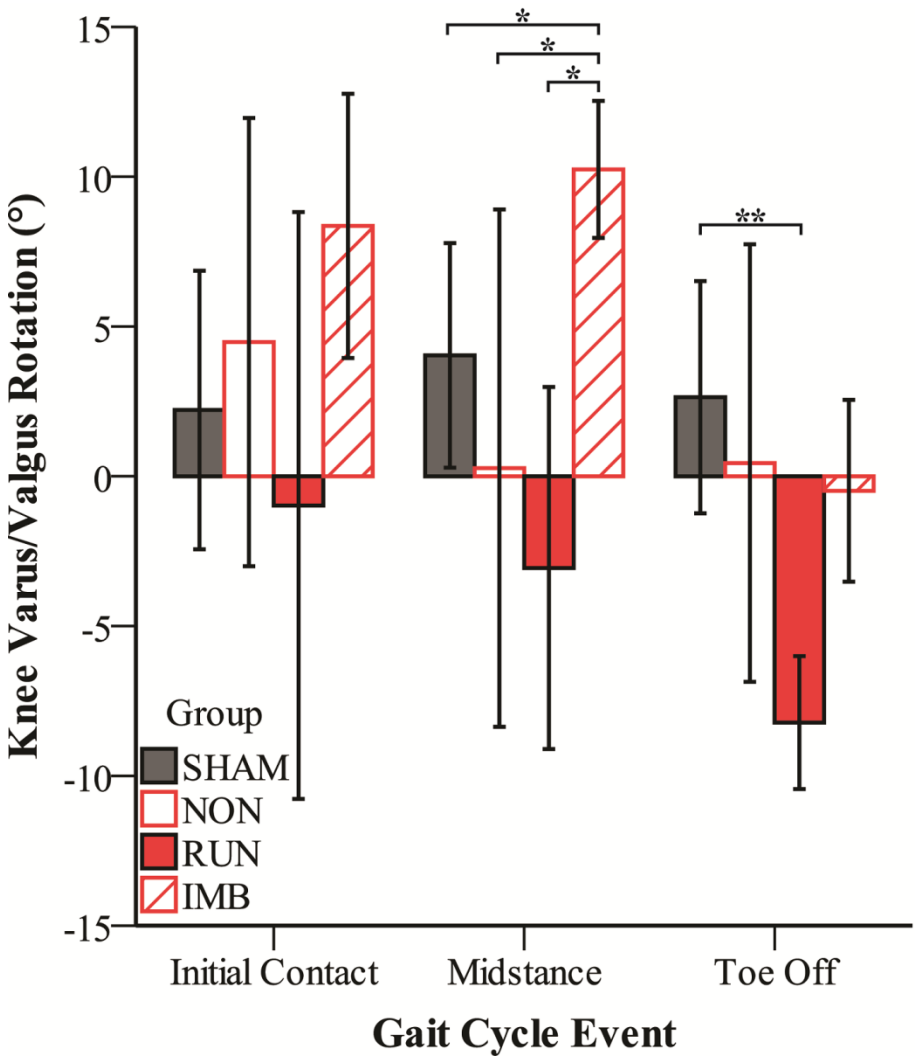

Figure C.4: Knee varus/valgus rotation (mean ± SD) quantified using Autoscoper. * = p < 0.10, ** = p < 0.05. 0° indicates no varus or valgus rotations

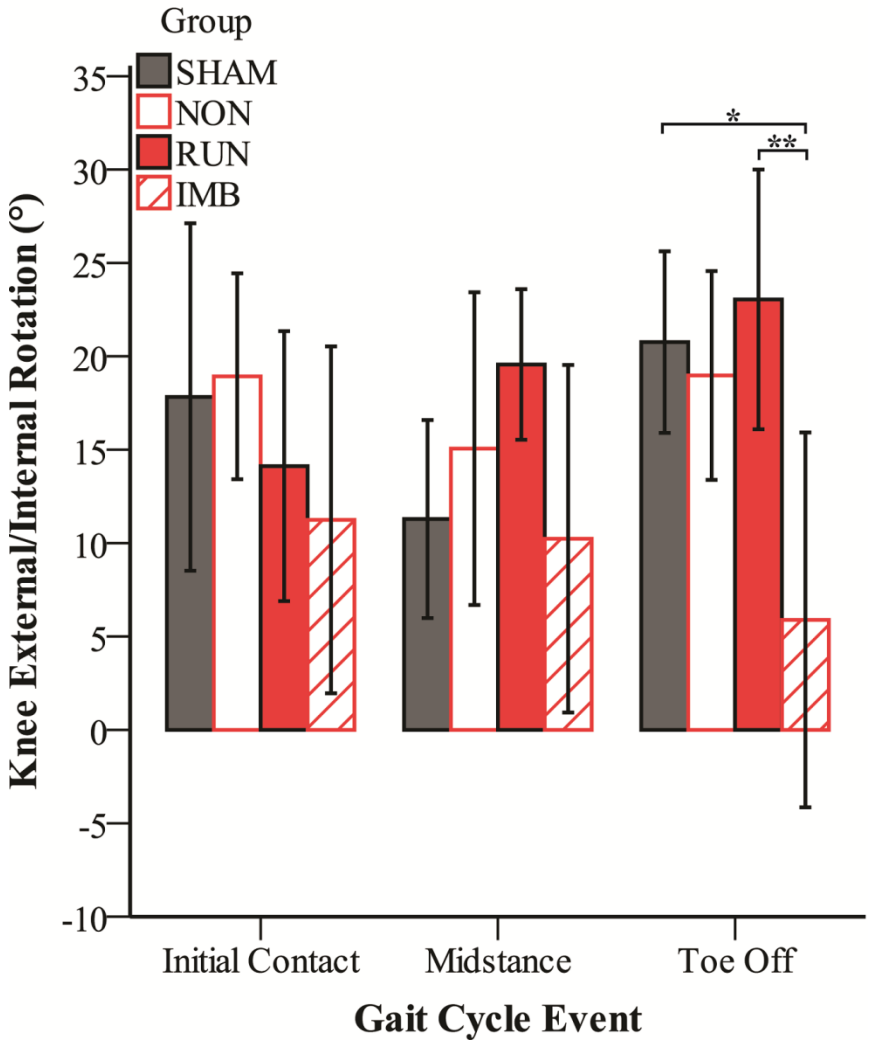

Figure C.5: Knee external/internal rotation (mean ± SD) quantified using Autoscoper. * = p < 0.10, ** = p < 0.05. 0° indicates no tibial rotation

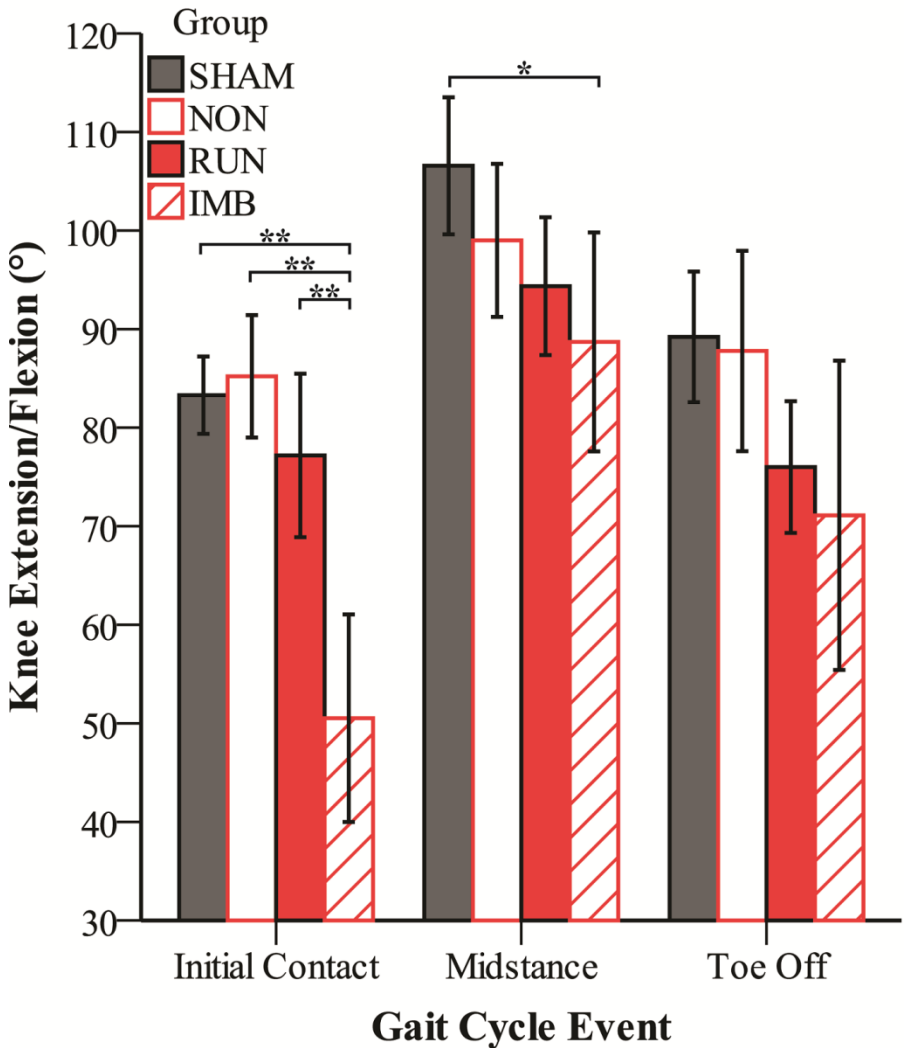

Figure C.6: Knee extension/flexion (mean ± SD) quantified using Autoscoper. * = p < 0.10, ** = p < 0.05. 0° indicates a fully extended tibia and fibula

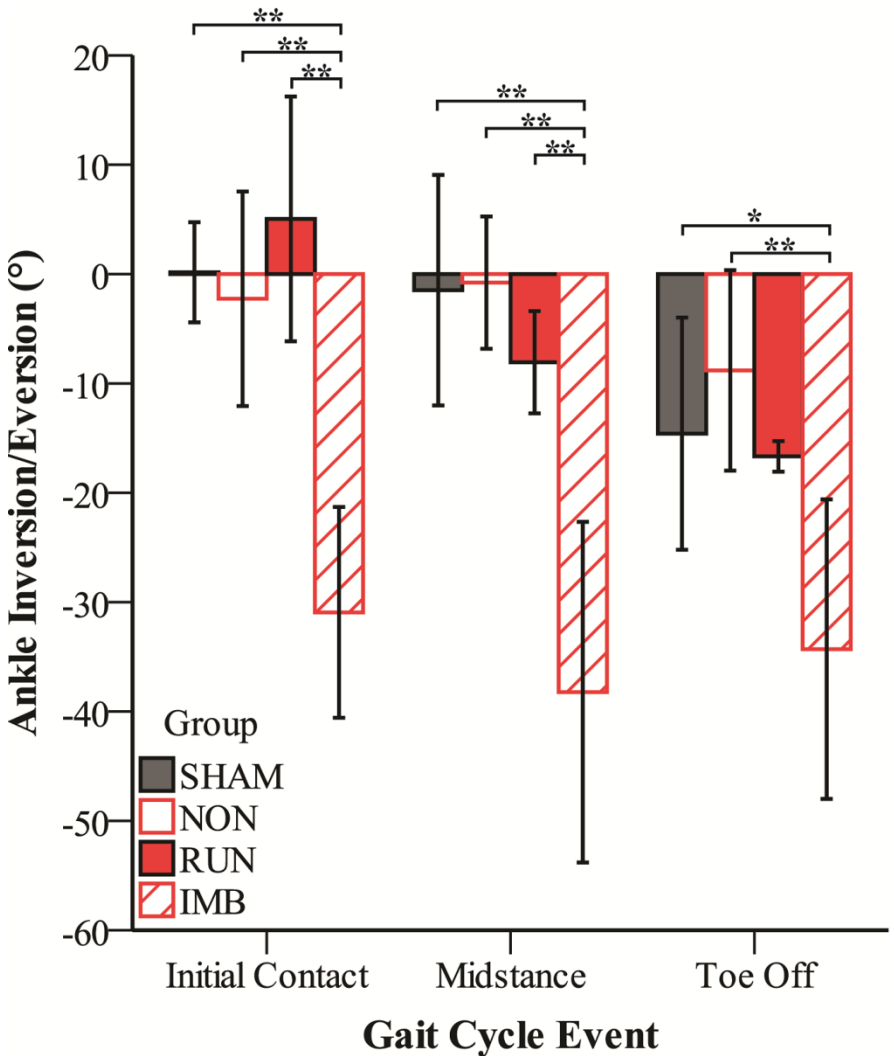

Figure C.7: Ankle inversion/eversion (mean ± SD) quantified using Autoscoper. * = p < 0.10, ** = p < 0.05. 0° indicates no inversion or eversion

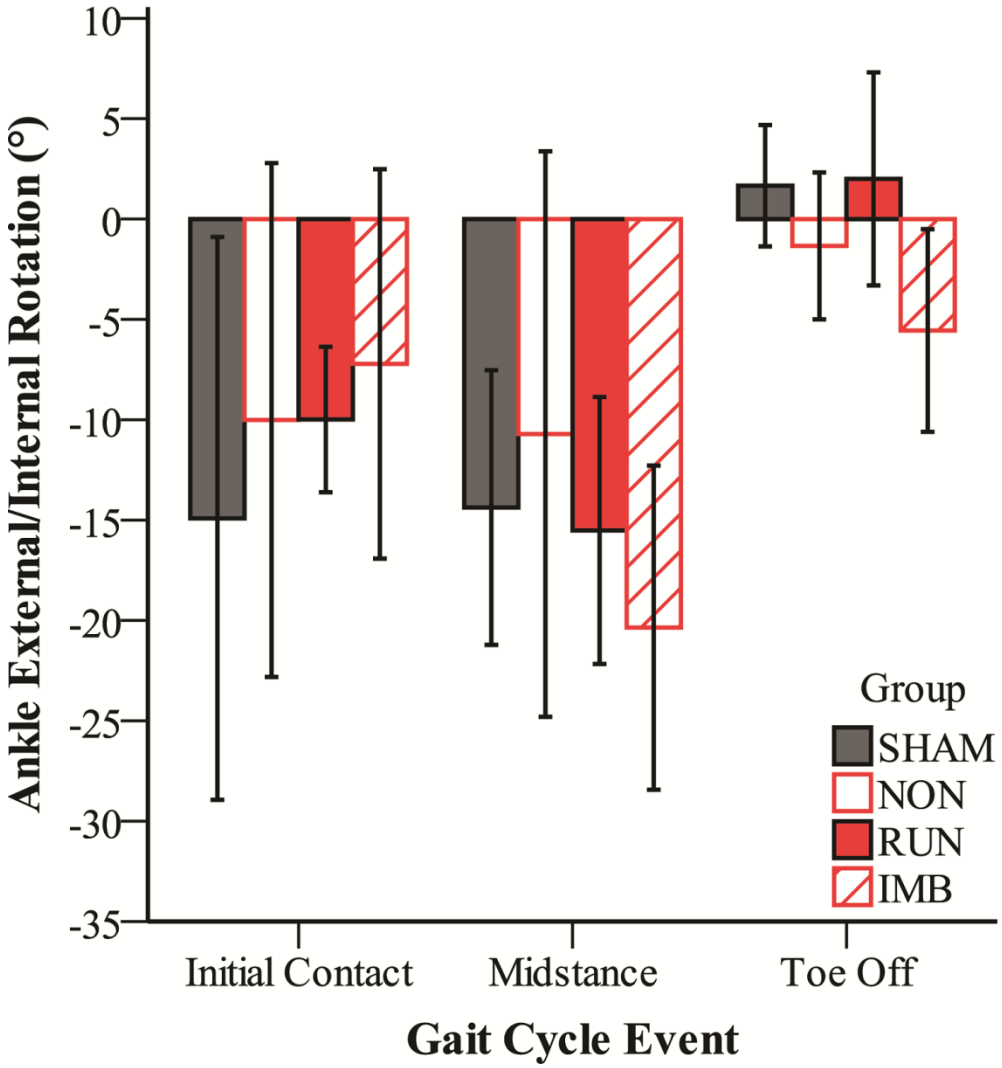

Figure C.8: Ankle external/internal rotation (mean ± SD) quantified using Autoscoper. * = p < 0.10, ** = p < 0.05. 0° indicates the foot is oriented forward

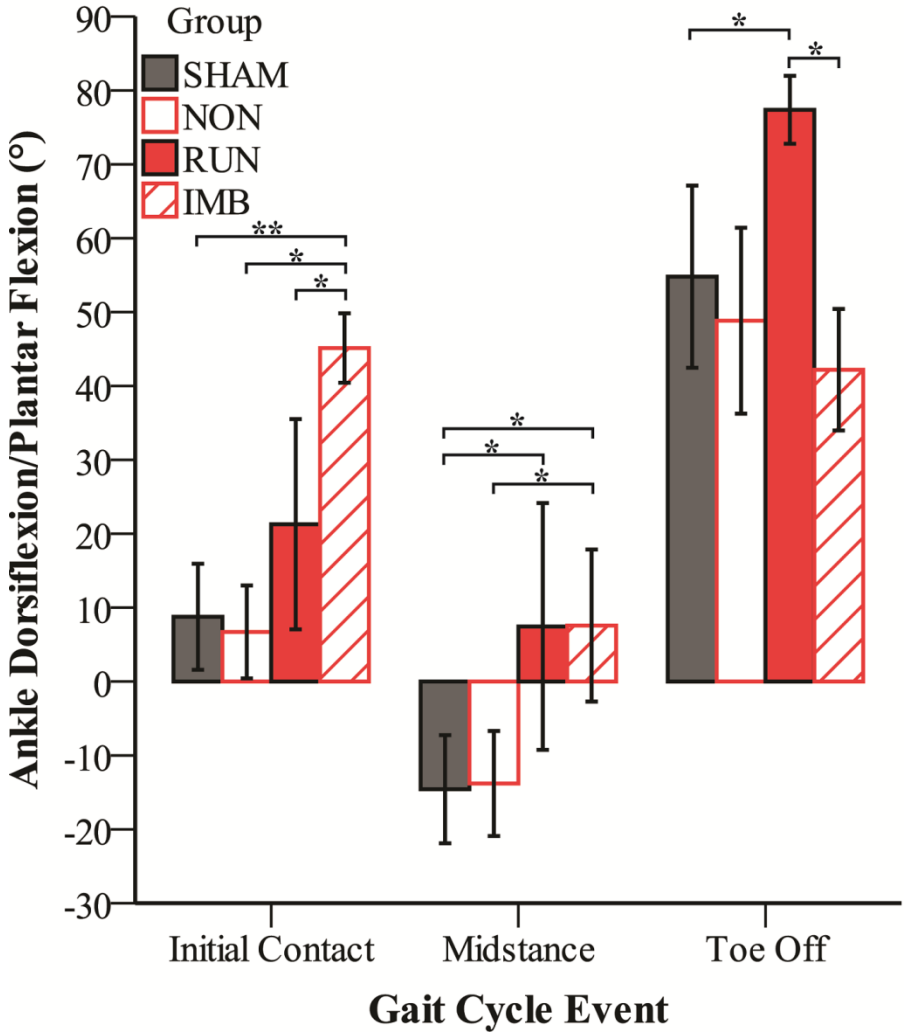

Figure C.9: Ankle dorsiflexion/plantar flexion (mean ± SD) quantified using Autoscoper. * = p < 0.10, ** = p < 0.05. 0° indicates the foot is perpendicular to the tibia and fibula

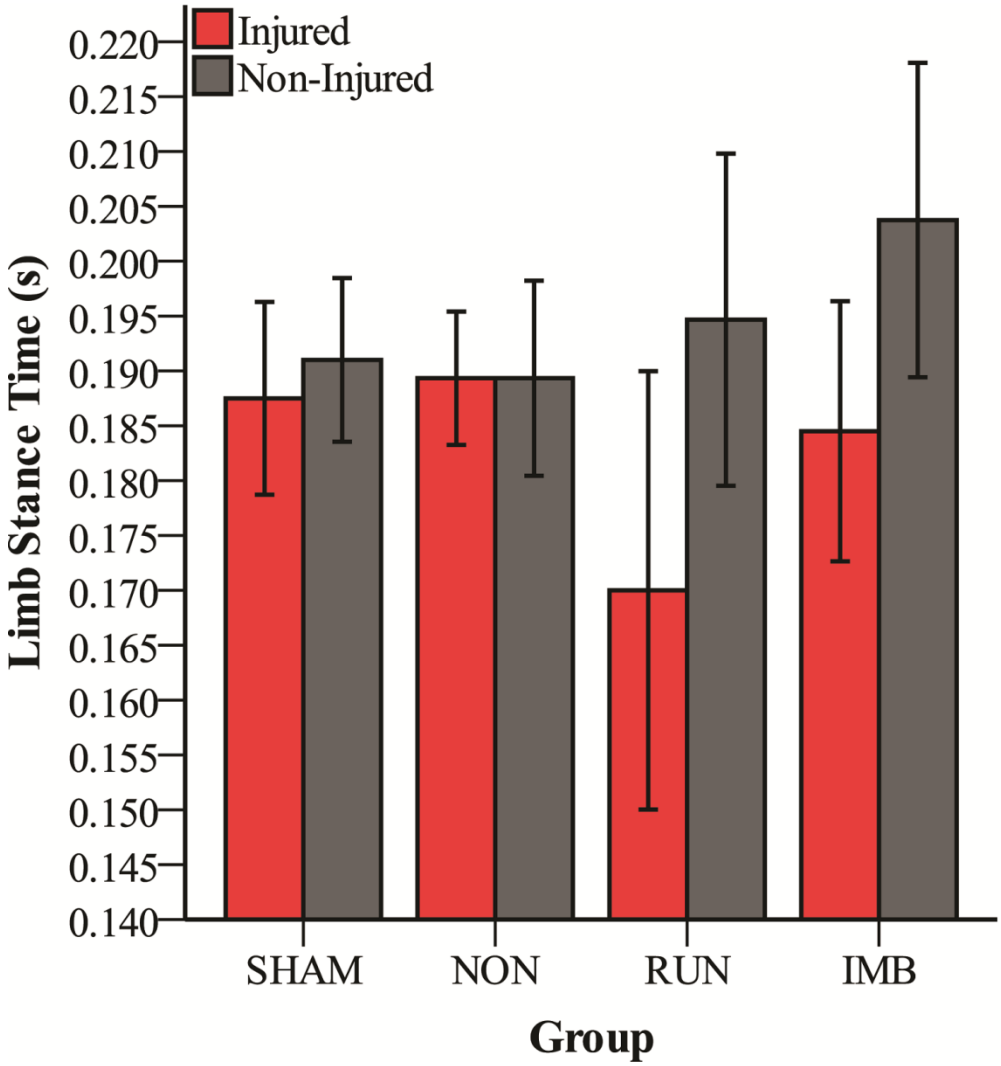

Figure C.10: Limb stance time (mean ± SD) for both the injured (left) and non-injured (right) legs. * = p < 0.10, ** = p < 0.05. Values indicate amount of time the limb is in contact with the ground during a single stride

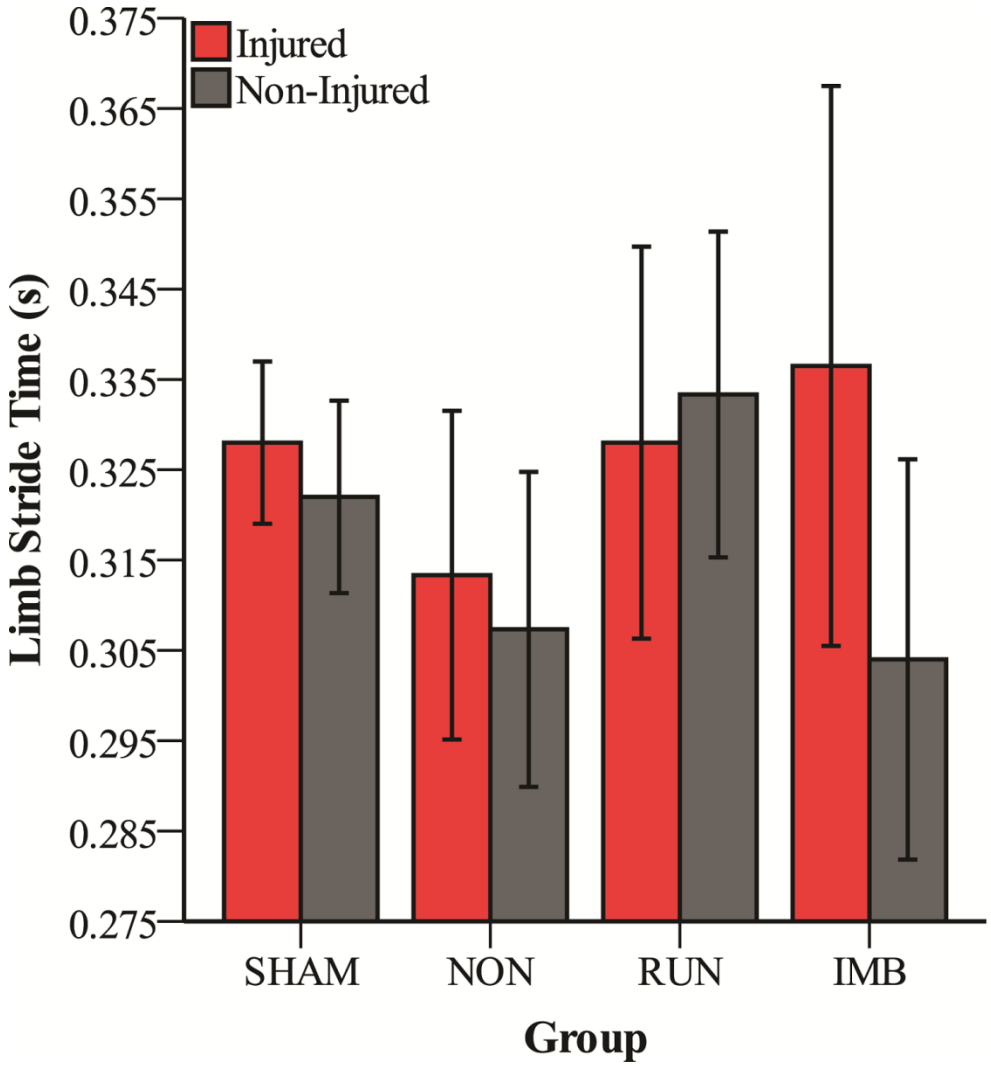

Figure C.11: Limb stride time (mean ± SD) for both the injured (left) and non-injured (right) legs. * = p < 0.10, ** = p < 0.05. Values indicate amount of time taken for the limb to go from one initial contact to the next initial contact

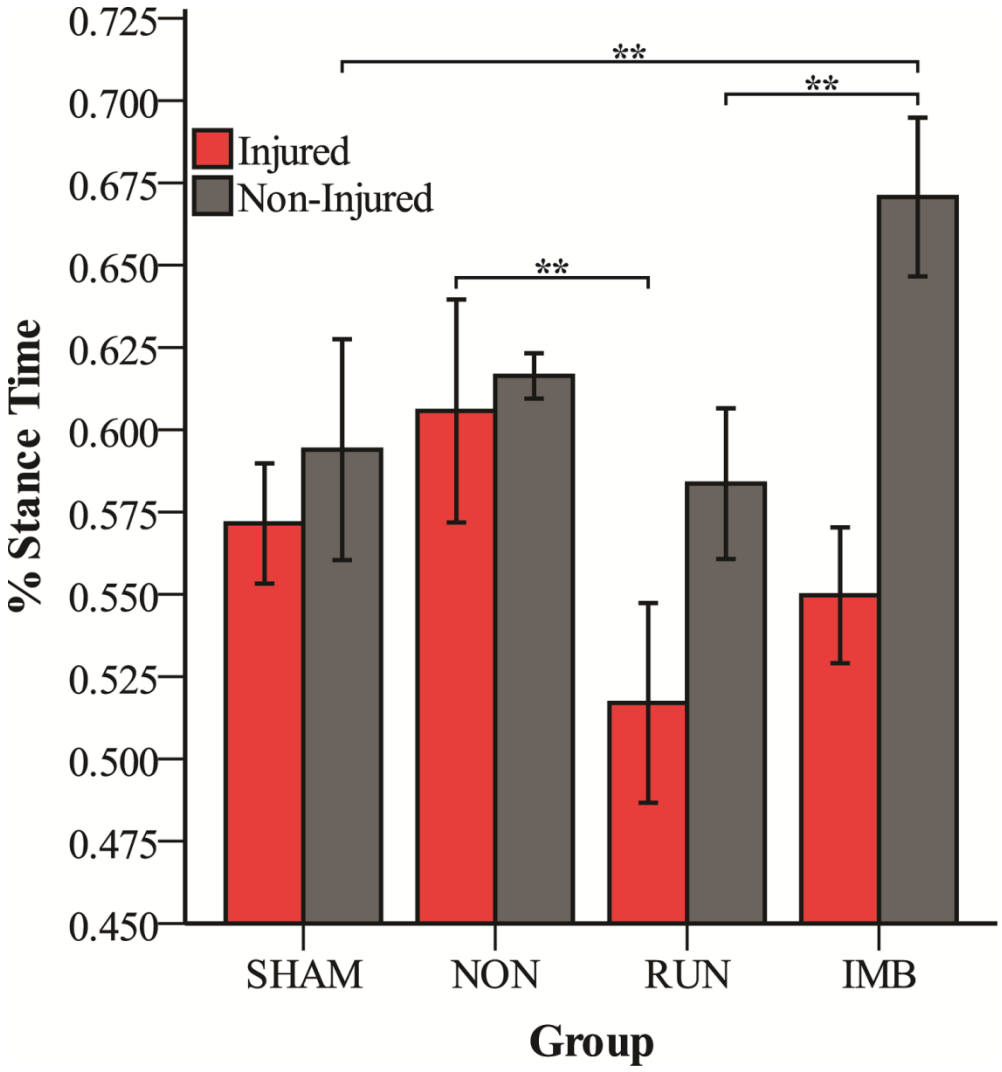

Figure C.12: Percentage stance time (mean ± SD) for both the injured (left) and non-injured (right) legs. * = p < 0.10, ** = p < 0.05. Values indicate amount of time the limb is in contact with the ground as a percentage of the stride time

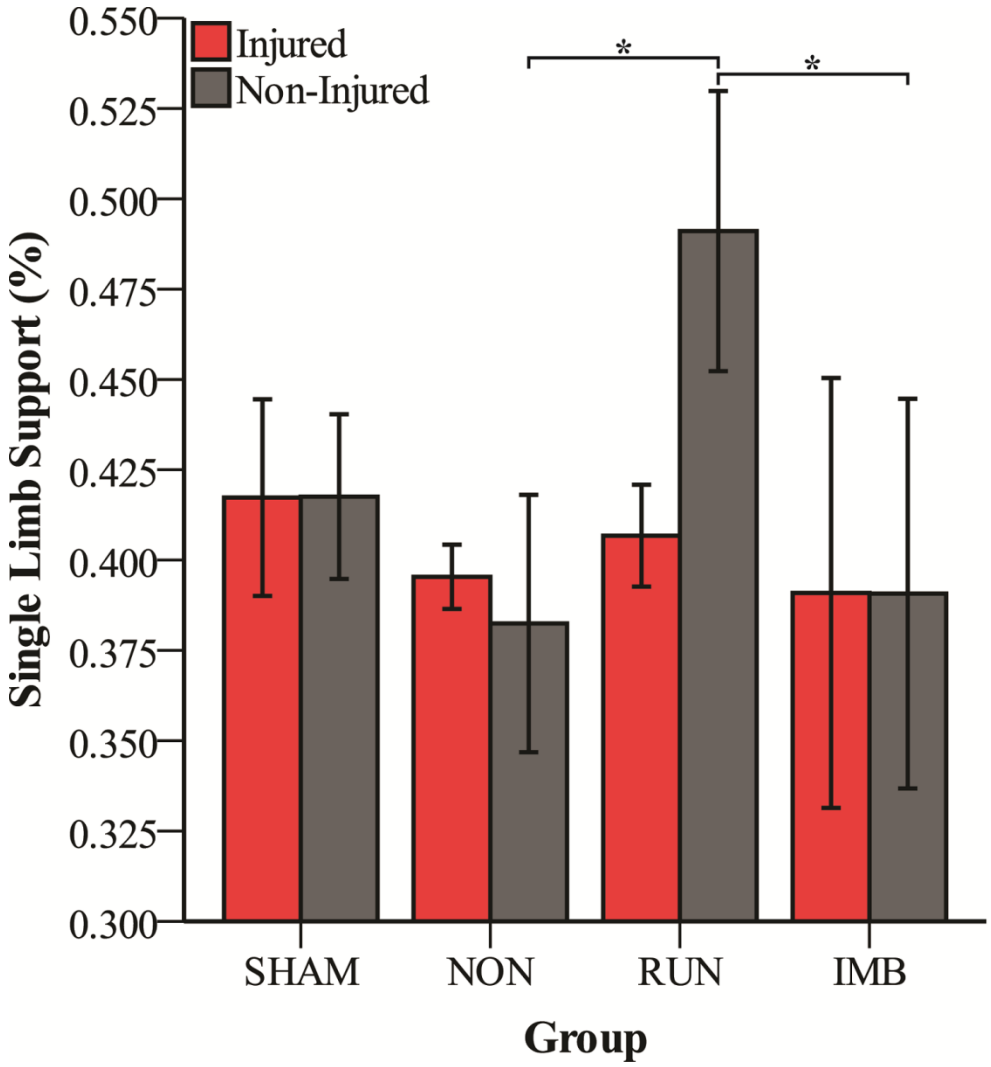

Figure C.13: Single limb support (mean ± SD) for both the injured (left) and non-injured (right) legs. * = p < 0.10, ** = p < 0.05. Values indicate amount of time the limb is in contact with the ground while the contralateral limb is not, as a percentage of stride time

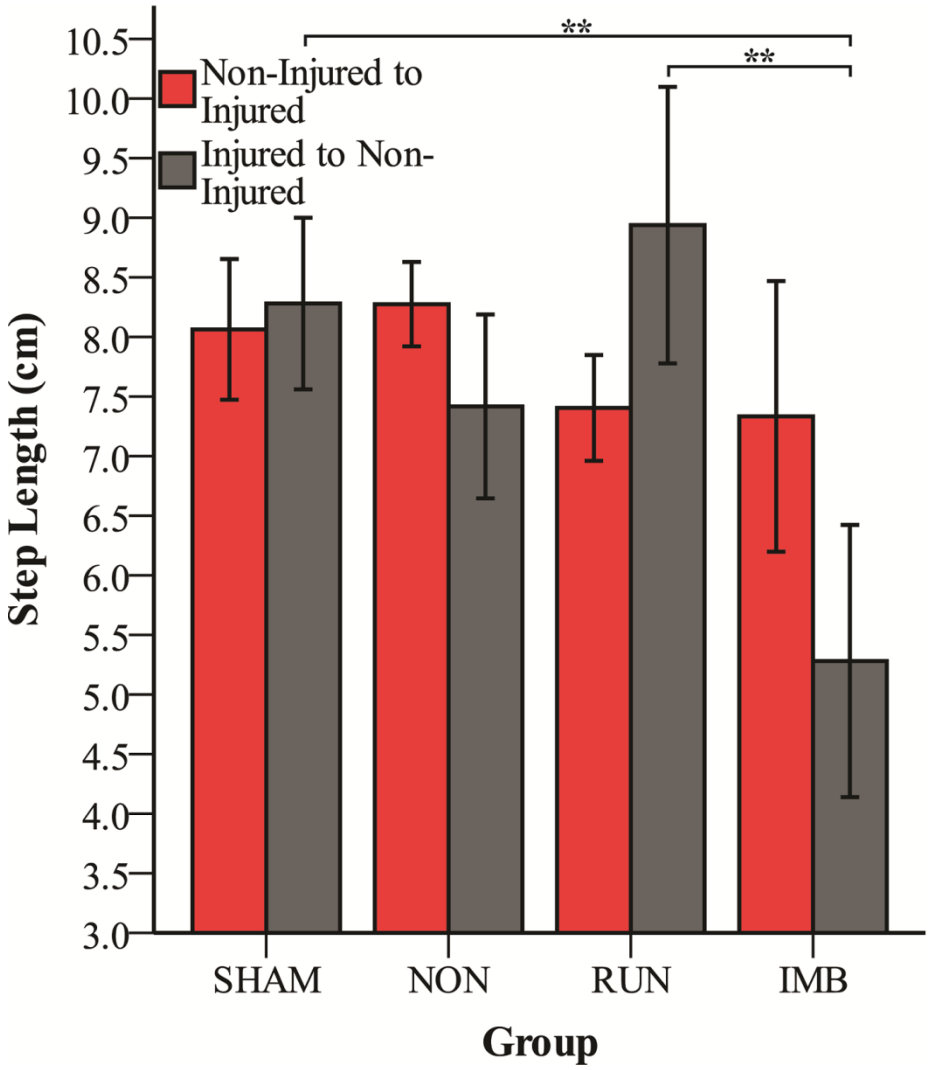

Figure C.14: Step length (mean ± SD) for both the injured to non-injured (left to right) and non-injured to injured (right to left) steps. * = p < 0.10, ** = p < 0.05. Values indicate amount of distance covered during the specified step, based on the "forward" vector

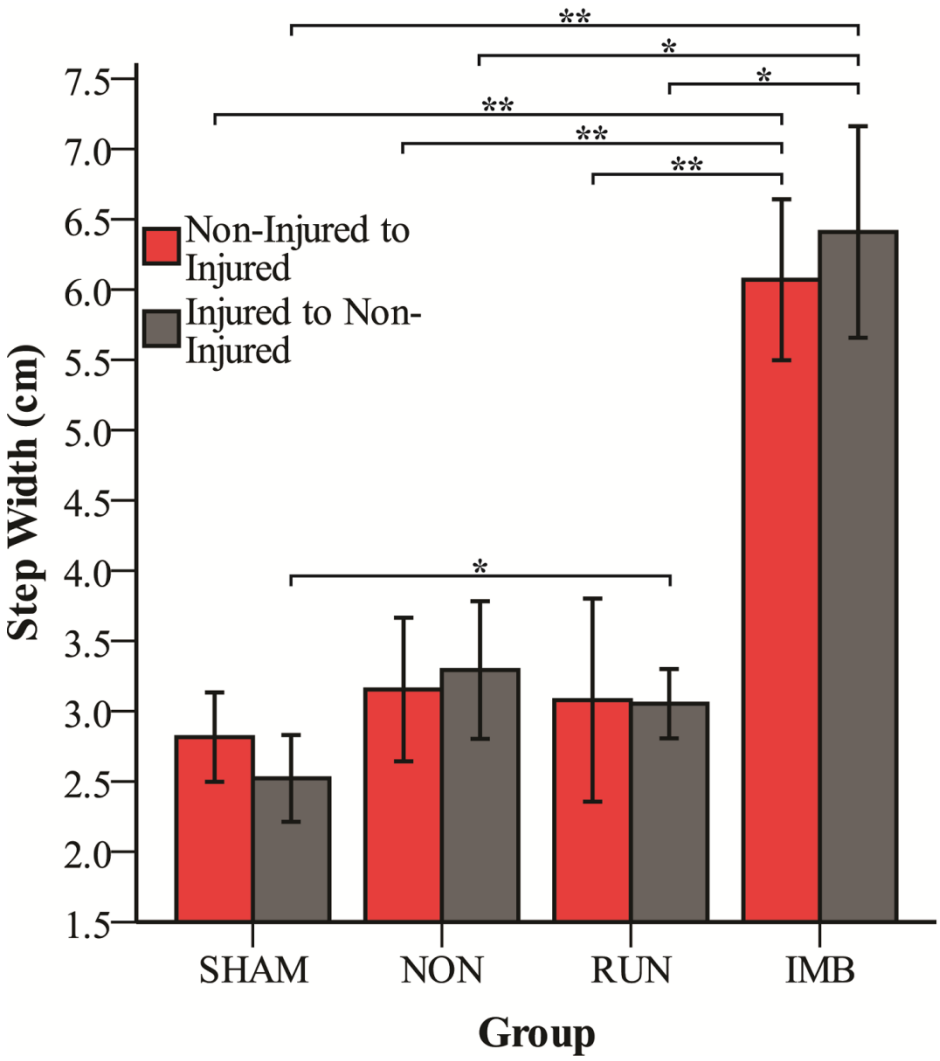

Figure C.15: Step width (mean ± SD) for both the injured to non-injured (left to right) and non-injured to injured (right to left) steps. * = p < 0.10, ** = p < 0.05. Values indicate amount of distance covered during the specified step, based on the vector perpendicular to the "vertical" and "forward" vectors

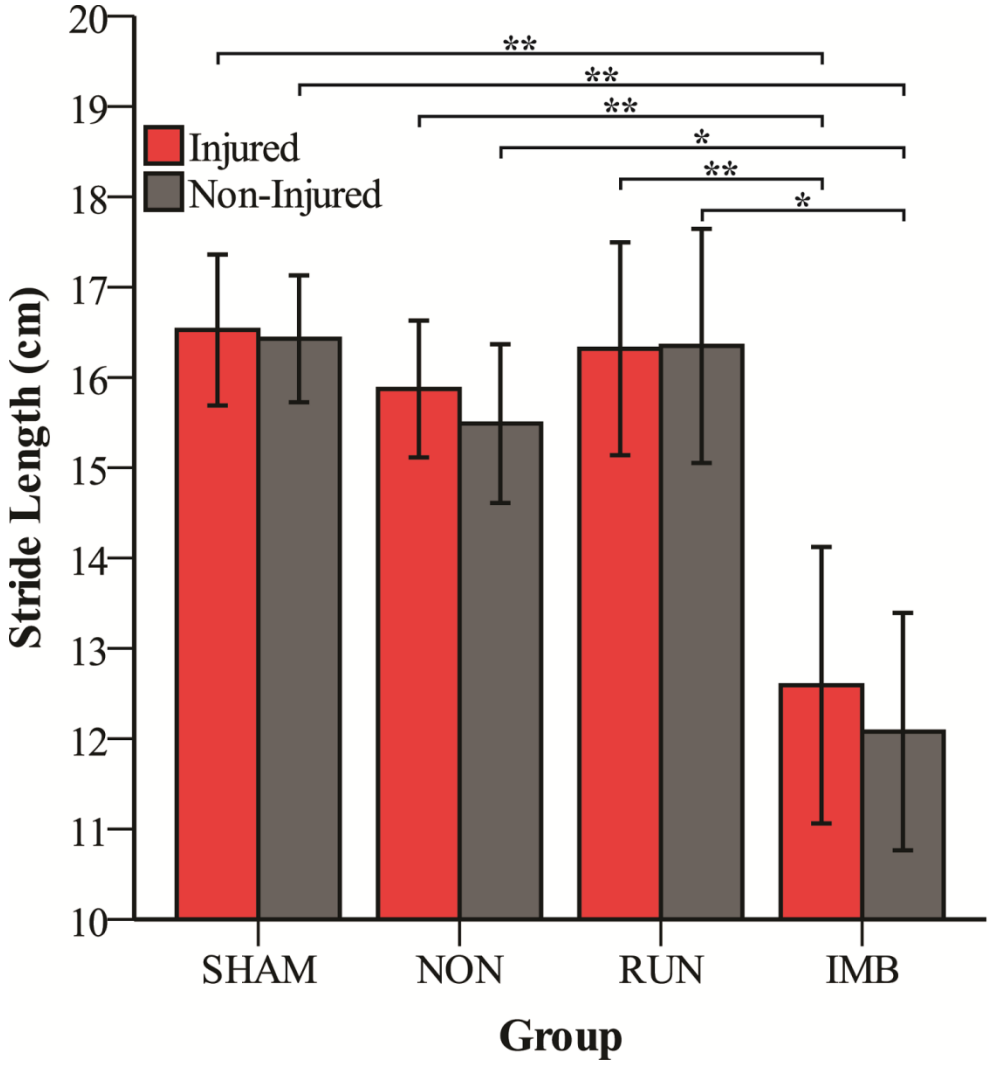

Figure C.16: Stride length (mean ± SD) for both the injured (left) and non-injured (right) legs. * = p < 0.10, ** = p < 0.05. Values indicate amount of distance covered during a single stride, based on the "forward" vector

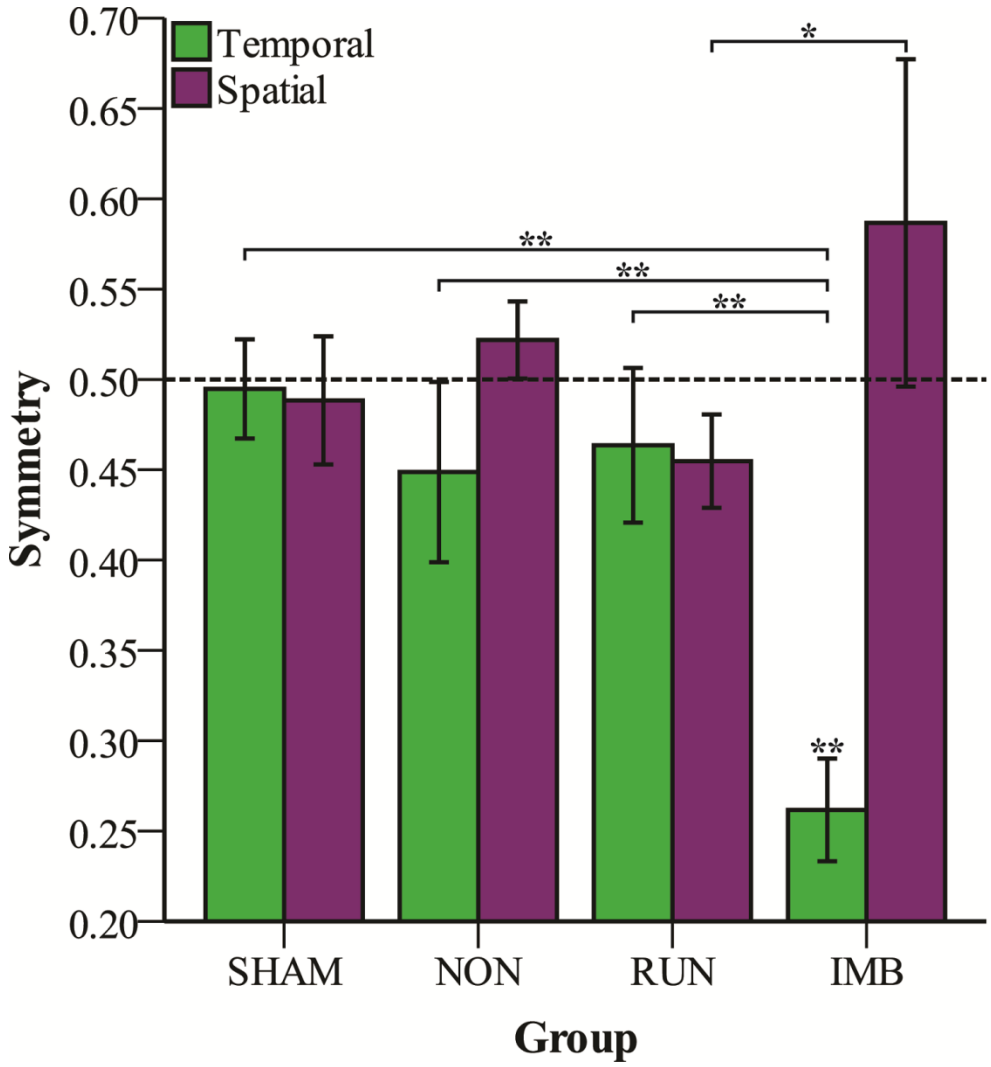

Figure C.17: Gait symmetry (mean ± SD) both spatially and temporally. Symmetry values of 0.50 indicate the right foot initial contact occurs exactly halfway through a left foot stride, in length or time respectively. * = p < 0.10, ** = p < 0.05

REFERENCES

[1] K. M. Jordan, N. K. Arden, M. Doherty, B. Bannwarth, J. W. J. Bijlsma, P. Dieppe, K. Gunther and M. Dougados, "EULAR Recommendations 2003: an evidence based approach to the management of knee osteoarthritis: Report of a Task Force of the Standing Committee for International Clinical Studies Including Therapeutic Trials (ESCISIT)," *Annals of the Rheumatic Diseases,* vol. 62, no. 12, pp. 1145-1155, 2003.

[2] V. Kumar, A. K. Abbas, N. Fausto and R. N. Mitchell, Robbins Basic Pathology, Philadelphia: Saunders Elsevier, 2007.

[3] D. T. Felson, R. C. Lawrence, P. A. Dieppe, R. Hirsch, C. G. Helmick and J. M. Jordan, "Osteoarthritis: New Insights. Part 1: The Disease and Its Risk Factors," *Annals of Internal Medicine,* vol. 133, no. 8, pp. 635-646, 2000.

[4] D. T. Felson, A. Naimark, J. Anderson, L. Kazis, W. Castelli and R. F. Meenan, "The Prevalence of Knee Osteoarthritis in the Elderly - The Framingham Osteoarthritis Study," *Arthritis and Rheumatism,* vol. 30, no. 8, pp. 914-918, 1987.

[5] J. L. Astephen, K. J. Deluzio, G. E. Caldwell and M. J. Dunbar, "Biomechanical changes at the hip, knee, and ankle joints during gait are associated with knee osteoarthritis severity," *Journal of Orthopaedic Research,* vol. 26, no. 3, pp. 332-341, 2008.

[6] J. Perry and J. M. Burnfield, Gait analysis: normal and pathological function, Thorofare: SLACK Incorporated, 2010.

[7] W. Zhang, R. W. Moskowitz, G. Nuki, S. Abramson, R. D. Altman, N. Arden, S. Bierma-Zeinstra, K. D. Brandt and P. Croft, "OARSI recommendations for the management of hip and knee osteoarthritis, Part II: OARSI evidence-based, expert consensus guidelines," *Osteoarthritis and Cartilage,* vol. 16, no. 2, pp. 137-162, 2008.

[8] A. M. Bendele, "Animal models of osteoarthritis," *Journal of Musculoskeletal Neuronal Interactions,* vol. 1, no. 4, pp. 363-376, 2001.

[9] M. H. Gregory, N. Capito, K. Kuroki, A. M. Stoker, J. L. Cook and S. L. Sherman, "A Review of Translational Animal Models for Knee Osteoarthritis," *Arthritis,* vol. 2012, p. 14, 2012.

[10] K. D. Allen, B. A. Mata, M. A. Gabr, J. L. Huebner, S. B. Adams, V. B. Kraus, D. O. Schmitt and L. A. Setton, "Kinematic and dynamic gait compensations resulting from knee instability in a rat model of osteoarthritis," *Arthritis Research & Therapy,* vol. 14, p. R78, 2012.

[11] H. E. Kloefkorn, B. Y. Jacobs, A. M. Loye and K. D. Allen, "Spatiotemporal gait compensations following medial collateral ligament and medial meniscus injury in the rat: correlating gait patterns to joint damage," *Arthritis Research & Therapy,* vol. 17, p. 287, 2015.

[12] J. Beckett, W. Jin, M. Schultz, A. Chen, D. Tolbert, B. R. Moed and Z. Zhang, "Excessive running induces cartilage degeneration in knee joints and alters gait of

rats," *Journal of Orthopaedic Research,* vol. 30, no. 10, pp. 1604-1610, 2012.

[13] A. Ando, H. Suda, Y. Hagiwara, Y. Onoda, E. Chimoto, Y. Saijo and E. Itoi, "Reversibility of Immobilization-Induced Articular Cartilage Degeneration after Remobilization in Rat Knee Joints," *Tohoku Journal of Experimental Medicin,* vol. 224, no. 2, pp. 77-85, 2011.

[14] B. Vanwanseele, E. Lucchinetti and E. Stussi, "The effects of immobilization on the characteristics of articular cartilage: current concepts and future directions," *Osteoarthritis and Cartilage,* vol. 10, pp. 408-419, 2002.

[15] C. B. Little and M. M. Smith, "Animal Models of Osteoarthritis," *Current Rheumatology Reviews,* vol. 4, no. 3, pp. 175-182, 2008.

[16] B. Y. Jacobs, H. E. Kloefkorn and K. D. Allen, "Gait Analysis Methods for Rodent Models of Osteoarthritis," *Current Pain and Headache Reports,* vol. 18, p. 456, 2014.

[17] K. A. Clarke, S. A. Heitmeyer, A. G. Smith and Y. O. Taiwo, "Gait Analysis in a Rat Model of Osteoarthritis," *Physiology & Behavior,* vol. 62, no. 5, pp. 951-954, 1997.

[18] C. E. Ferland, S. Laverty, F. Beaudry and P. Vachon, "Gait analysis and pain response of two rodent models of osteoarthritis," *Pharmacology, Biochemistry and Behavior,* vol. 97, pp. 603-610, 2011.

[19] J. M. Bauman and Y.-H. Chang, "High-speed X-ray video demonstrates significant skin movement errors with standard optical kinematics during rat locomotion," *Journal of Neuroscience Methods,* vol. 186, pp. 18-24, 2010.

[20] M. K. Boettger, J. Leuchtweis, H.-G. Schaible and M. Schmidt, "Videoradiographic analysis of the range of motion in unilateral experimental knee joint arthritis in rats," *Arthritis Research & Therapy,* vol. 13, p. R79, 2011.

[21] S. M. Gatesy, D. B. Baier, F. A. Jenkins and K. P. Dial, "Scientific Rotoscoping: A Morphology-Based Method of 3-D Motion Analysis and Visualization," *Journal of Experimental Zoology,* vol. 313A, no. 5, pp. 244-261, 2010.

[22] B. J. Fregly, H. A. Rahman and S. A. Banks, "Theoretical Accuracy of Model-Based Shape Matching for Measuring Natural Knee Kinematics with Single-Plane Fluoroscopy," *Journal of Biomechanical Engineering,* vol. 127, no. 4, pp. 692-699, 2005.

[23] E. L. Brainerd, D. B. Baier, S. M. Gatesy, T. L. Hedrick, K. A. Metzger, S. L. Gilbert and J. J. Crisco, "X-ray Reconstruction of Moving Morphology (XROMM): Precision, Accuracy and Application in Comparative Biomechanics Research," *Journal of Experimental Zoology,* vol. 313A, no. 5, pp. 262-279, 2010.

[24] D. L. Miranda, J. B. Schwartz, A. C. Loomis, E. L. Brainerd, B. C. Fleming and J. J. Crisco, "Static and Dynamic Error of a Biplanar Videoradiography System Using Marker-Based and Markerless Tracking Techniques," *Journal of Biomechanical Engineering,* vol. 133, no. 12, pp. 121002-121002-8, 2011.

[25] J. Wang and T. J. Blackburn, "X-ray Image Intensifiers for Fluoroscopy," *Radiographics,* vol. 20, no. 5, pp. 1471-1477, 2000.

[26] B. J. Knorlein, D. B. Baier, S. M. Gatesy, J. D. Laurence-Chasen and E. L. Brainerd,

"Validation of XMALab software for marker-based XROMM," *Journal of Experimental Biology,* vol. 219, no. 23, pp. 3701-3711, 2016.

[27] LEGO, "Company Profile 2009," 2009. [Online]. Available: cache.lego.com/downloads/aboutus/LEGO_company_profile_UK.pdf.

[28] M. F. Bonnan, J. Shulman, R. Varadharajan, C. Gilbert, M. Wilkes, A. Horner and E. Brainerd, "Forelimb Kinematics of Rats Using XROMM, with Implications for Small Eutherians and Their Fossil Relatives," *PLoS ONE,* vol. 11, no. 3, 2016.

[29] A. Davidson, E. S. Gardinier and D. H. Gates, "Within and between-day reliability of energetic cost measures during treadmill walking," *Cogent Engineering,* vol. 3, no. 1, 2016.

[30] R. E. Kambic, T. J. Roberts and S. M. Gatesy, "Long-axis rotation: a missing degree of freedom in avian bipedal locomotion," *Journal of Experimental Biology,* vol. 217, no. 15, pp. 2770-2782, 2014.

[31] W. L. Johnson, D. L. Jindrich, R. R. Roy and V. R. Edgerton, "A three-dimensional model of the rat hindlimb: Musculoskeletal geometry and muscle moment arms," *Journal of Biomechanics,* vol. 41, no. 3, pp. 610-619, 2008.

[32] T. J. Burkholder and T. R. Nichols, "Three-dimensional model of the feline hindlimb," *Journal of Morphology,* vol. 261, no. 1, pp. 118-129, 2004.

[33] M. Hildebrand, "The Quadrupedal Gaits of Vertebrates," *Bioscience,* vol. 39, no. 11, pp. 766-775, 1989.